Chapter 2

EXPERIMENTS

2.1 Technological Candidates for Quantum Computers

To date—about ten years after the first experimental implementation of one qubit—most of the numerous proposals for quantum computing prototypes have not been able to implement more than one or two qubits. Thus, one still cannot single out a most promising technological candidate for a future quantum computer. This situation does not mean, however, that there are doubts about whether to pursue the experimental efforts further. The quantum computer project is taken as inevitable, and the experimental efforts have been undertaken and supported with a vigor similar to the efforts dedicated to the nuclear fusion program from the 1960s till today.

Both these projects appear to be unstoppable multi-billion dollar international initiatives (in 2004 the United States dropped its own fusion research project, FIRE, in favor of concentrating all resources on the international ITER project), but the quantum information processing project may have a better chance of success. There are several reasons for this. The nuclear fusion project is not perceived as being able to lead to a practical commercial power plant in the near future, even if the project turns out to be successful in the end, while an operating quantum computer would have no such problems, however complicated and expensive it would be. Moreover, the main classical computer producers increasingly support both theoretical and experimental quantum information groups. From the very beginning, nuclear fusion experiments and their financial support were mostly concentrated on the *tokamak*. In contrast, there is an increasing variety of comparatively low-cost

platforms for quantum computers, and the financial support is spread evenly over a constantly growing number of experimental and theoretical groups throughout the world. Finally, nuclear fusion theory is basically a nuclear reaction theory tied mainly to the tokamak experiments, while quantum information theory is a true interdisciplinary project involving many specialties of physics, mathematics, and computer science. As a result, new jobs in quantum information field become available practically each day, and both quantum information theory and its experiments are having a growing impact on all the various fields from which they emerged.

At the beginning of this section, we mentioned that only a few technological candidates for future quantum computing platforms have succeeded in manipulating several qubits. These are nuclear magnetic resonance (NMR), with molecules in a liquid; ion traps; and cavity quantum electrodynamics (QED). In this chapter, we shall elaborate on the first two as well as a recently proposed silicon-based model. Then, in Sections 2.6 (p. 123) and 2.7 (p. 125), we shall briefly present a *quantum information science and technology roadmap* for quantum computation and communication, as well as some experimental details and perspectives of quantum cryptography setups.

2.2 Zeeman Effects

Qubits that we can prepare, manipulate, and measure are two-level states of photons, electrons, and nucleons. Apart from all-photon computers, electrons play an important role in understanding and designing quantum computers. In this section we therefore consider electron states. There are no "off the shelf" two-level states of electrons within atoms, since electron spins interact with their orbits and with the nuclei of the atoms. We can distinguish all the electron states only when atoms are in a magnetic field. This behavior is called the normal and anomalous electron Zeeman effect within atoms [Greiner, 1989]. We will review the Zeeman effects in this section, not because they work directly as quantum computing devices but because many details of quantum devices that we will elaborate on in the subsequent sections are based on or derived from them.

Let us consider an electron in the simplest possible atom (hydrogen) in the Bohr model. The electron is represented as a particle of mass m and charge $-e$ rotating around a proton of charge $+e$, as shown in Fig. 2.1(a).

The rotating charge forms a current

$$j = \frac{e}{t} = e\frac{v}{2\pi r}$$

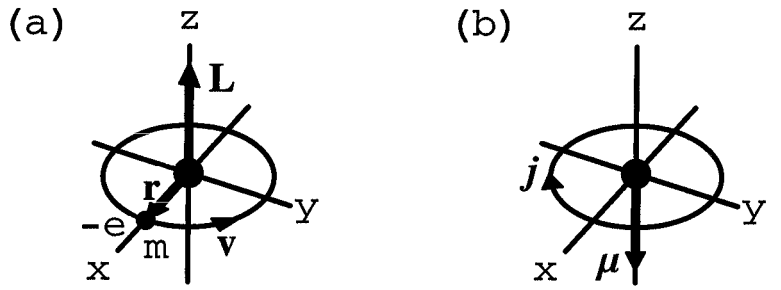

Figure 2.1. An electron rotating around a proton in the Bohr model.

and a *magnetic (dipole) moment*

$$\boldsymbol{\mu}_L = -jr^2\pi\boldsymbol{k} = -\frac{1}{2}e\mathbf{r}\times\mathbf{v} = -\frac{e}{2m}\mathbf{L}, \tag{2.1}$$

where $\boldsymbol{k}$ is the unit vector along the z-axis, $\mathbf{L}$ is the angular momentum of the electron, and m is the electron mass. Therefore, the electron carries a magnetic moment proportional to its angular momentum. Since this outcome is valid in general quantum mechanics, it is valid for the angular momentum operator and therefore not only for the orbital motion of the electron but also for its intrinsic spin angular momentum. The values of the angular momentum are determined by the *angular momentum quantum number*, l, and the values of its z-component by the *magnetic quantum number*, m_l:

$$L = \hbar\sqrt{l(l+1)}, \quad l = 0,\ldots,n-1, \quad L_z = m_l\hbar, \quad m_l = -l,\ldots,l, \tag{2.2}$$

where n is the main quantum number. Introducing $\mu_B = e\hbar/2m$, called the *Bohr magneton*, we can write Eq. (2.1) as

$$\boldsymbol{\mu}_L = -\frac{\mu_B}{\hbar}\mathbf{L}. \tag{2.3}$$

From Eq. (2.2) we also get

$$\mu_{lz} = -\mu_B m_l. \tag{2.4}$$

Similarly, for the electronic spin we have

$$S = \hbar\sqrt{s(s+1)}, \qquad S_z = m_s\hbar, \quad m_s = \pm\frac{1}{2}. \tag{2.5}$$

We do not have a good semiclassical picture for spin (an electron spinning around itself does not work), and therefore we can only conclude that

$$\boldsymbol{\mu}_S = -\frac{g_s e}{2m}\mathbf{S} = -\frac{g_s \mu_B}{\hbar}\mathbf{S}, \qquad \mu_{sz} = -g_s \mu_B m_s, \tag{2.6}$$

where g_s is called the *gyromagnetic factor* (see p. 46) We need another theory—quantum electrodynamics, QED—to determine it: $g_s = 2.002319304386$. We often take it to be 2.

The main idea behind manipulating qubits is to put them in an external field we can control and to get a response we can detect. For our atom, the field would be a uniform magnetic field $\mathbf{B}$ and the response would be spectral lines. In the magnetic field $\mathbf{B}$ oriented along the z-axis, the electron can have the following potential energies:

$$U_L = -\boldsymbol{\mu}_L \cdot \mathbf{B}, \qquad U_S = -g_s \boldsymbol{\mu}_S \cdot \mathbf{B}, \tag{2.7}$$

and from Eq. (2.4) we see that the energies of the electron are changed by the amounts

$$\Delta E_l = m_l \mu_B B, \qquad \Delta E_s = m_l g_s \mu_B B \tag{2.8}$$

from the value they had in the absence of the magnetic field ($B = 0$). This change can be detected by observing the splitting of the spectral lines. For instance, when an electron in an excited state 2p ($n = 2$, $l = 1$) within a hydrogen atom deexcites to the ground state 1s ($n = 1$, $l = 0$) via the emission of a photon, the photon will have only one spectral line, i.e., only one frequency. If we put the atom in a magnetic field, the so-called *normal Zeeman splitting* occurs following Eq. (2.8), as shown in Fig. 2.2.

We can see that there is always an odd number of levels and spectral lines, and therefore we cannot have a one-to-one correspondence between Zeeman levels and states of two-level systems that we need for quantum computation. We could look for just pairs of states as will do in Sec. 3.1.6 (p. 146), but this is not what we would call an off-the-shelf solution. If we try spins we can get an even level splitting, but things get complicated then. To see this let us again consider the semiclassical Bohr picture.

In a hydrogen atom, the electron circles around the proton; but in a system fixed to an electron, the proton circles around the electron and generates the following inner magnetic field at the position of the electron:

$$B_{\text{in}} = \mu_0 \frac{I}{2r} = \mu_0 \frac{e}{t}\frac{1}{2r} = \mu_0 \frac{e}{2r}\frac{v}{2r\pi} = \frac{\mu_0 e L}{4\pi m r^3}. \tag{2.9}$$

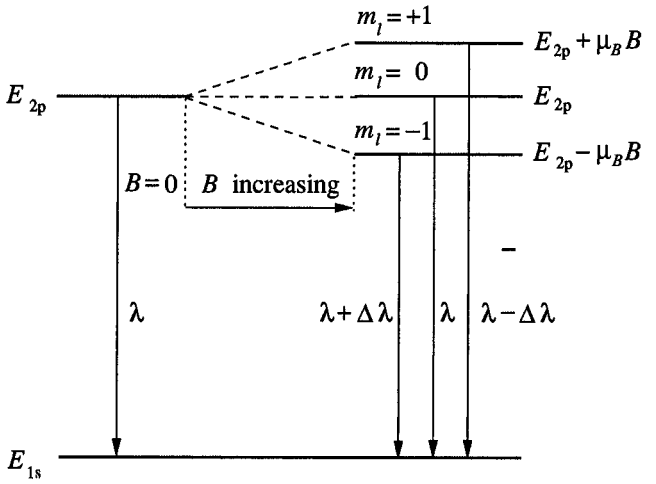

Figure 2.2. The normal Zeeman splitting.

The direction of this inner magnetic field generated by the orbital motion of the electron must be the direction of the angular momentum, **L**. Eqs. (2.9) and (2.6) give the following potential energy for the electron's spin:

$$U_J = -\boldsymbol{\mu}_S \cdot \mathbf{B}_{\text{in}} = \frac{\mu_0 e^2}{4\pi r^3 m^2}\mathbf{S}\cdot\mathbf{L} = \frac{e^2}{4\pi\epsilon_0 r^3 m^2 c^2}\mathbf{S}\cdot\mathbf{L}, \tag{2.10}$$

which is called the *spin–orbit interaction.* Comparing Eqs. (2.7) and (2.10), we interpret the spin–orbit interaction as an internal Zeeman effect. The spectral lines of the corresponding spontaneous emission are split into an *even* number of lines, as shown on the left-hand side of Fig. 2.3 for sodium.

Thus, what characterizes the electrons within an atom is the *total* angular momentum **J**:

$$\begin{aligned} &\mathbf{J} = \mathbf{L} + \mathbf{S}, \qquad J = \hbar\sqrt{j(j+1)} \qquad j = |l \pm s|, \\ &J_z = m_j\hbar, \qquad m_j = -j, -j+1, \ldots, j. \end{aligned} \tag{2.11}$$

The splitting of spectral lines under the influence of the external magnetic field is called the *anomalous* Zeeman effect and is shown in Fig. 2.3.

The magnetic moment and its z components are

$$\boldsymbol{\mu}_J = -\frac{e}{2m}\mathbf{J}, \qquad \mu_{jz} = -g\mu_B m_j, \tag{2.12}$$

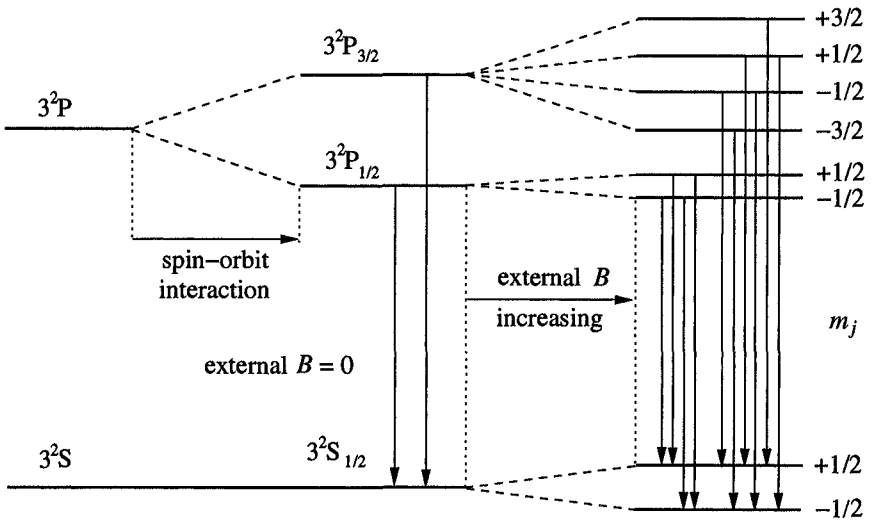

Figure 2.3. The spin–orbit interaction of sodium splits 3^2P into $3^2P_{3/2}$ and $3^2P_{1/2}$, and the external magnetic field splits these and the ground state 3^2S further into the lines shown on the right (ΔE shifts). The selection rules $\Delta j = 0$ ($j \neq 0$), ± 1, $\Delta m_j = 0, \pm 1$, give the spectral lines—an anomalous Zeeman effect.

where

$$g = 1 + \frac{j(j+1) + s(s+1) - l(l+1)}{2j(j+1)} \tag{2.13}$$

is called the *Landé factor* [Greiner, 1989]. The potential energy of the electron in the field is

$$U_J = -\boldsymbol{\mu}_J \cdot \mathbf{B}. \tag{2.14}$$

Due to this magnetic moment, by putting atoms into the magnetic field $\mathbf{B}$, the following energy shift occurs between $B = |\mathbf{B}| = 0, j$ level, and $B \neq 0, j, m_j$ level:

$$\Delta E_j = g m_j \mu_B B. \tag{2.15}$$

However, in deriving this equation [as well as Eq. (2.8)] we assumed that $\mathbf{J}$ ($\mathbf{L}$) is aligned with $\mathbf{B}$. For Eqs. (2.1), (2.12), (2.7), and (2.14) show that when $\mathbf{J}$ ($\mathbf{L}$) is perpendicular to $\mathbf{B}$ we have $U = \Delta E = 0$. $\mathbf{J}$ can be oriented in any direction when we switch on $\mathbf{B}$, and then $\mathbf{B}$ acts on the electron with torque

$$\boldsymbol{\tau}_J = \boldsymbol{\mu}_J \times \mathbf{B} = -g\mu_B \mathbf{J} \times \mathbf{B}. \tag{2.16}$$

If we neglect the spin–orbit interaction, we then have

$$\boldsymbol{\tau}_L = -\mu_B \mathbf{L} \times \mathbf{B} \qquad \text{and} \qquad \boldsymbol{\tau}_S = -g_S \mu_B \mathbf{S} \times \mathbf{B}. \tag{2.17}$$

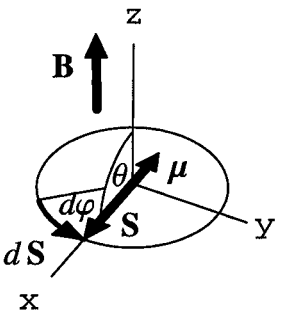

Figure 2.4. Electron with spin precessing in a magnetic field $\mathbf{B}$. $\theta = \pi/2$ is chosen although θ can have any value between 0 and π.

The torques will cause changes in the directions of $\mathbf{L}$ and $\mathbf{S}$:

$$\boldsymbol{\tau}_L = -\frac{d\mathbf{L}}{dt}, \qquad \boldsymbol{\tau}_S = -\frac{d\mathbf{S}}{dt} \tag{2.18}$$

that amount to precession about $\mathbf{B}$, which frequencies, called *Larmor (angular) frequencies*, are (see Fig. 2.4)

$$\omega_L = \frac{d\phi}{dt} = \frac{|d\mathbf{L}/dt|}{L\sin\theta} = \frac{eLB\sin\theta}{L\sin\theta} = \frac{\mu_B}{\hbar}B, \qquad \omega_S = \frac{g_S\mu_B}{\hbar}B. \tag{2.19}$$

Note that $\omega_S \approx 2\omega_L$. The term *Larmor frequency* is also often used for $\nu = \frac{\omega}{2\pi}$.

Using the Planck formula $E = h\nu = \hbar\omega$, we see that the obtained frequencies give energies that are exactly the energy shifts (2.8) and therefore correspond to high frequencies (electron Larmor frequency, ν for 1 Tesla magnetic field is 28.025 GHz). This means that the detection of such energies for two-level systems, i.e., for spin 1/2 qubits, would be difficult—regardless of whether we attempt to carry out direct detection of the precession energies or indirect detection through the Zeeman splitting of the spontaneous emissions. Then the spontaneous transitions occur within very short time intervals (10^{-8}–10^{-4} sec). In the end, electron spin states are always "screened" by the spin–orbit interaction as well as by the electron interaction with the nucleus, which is several orders of magnitude more massive than electrons.

Nonetheless, we have enough elements to design a system that could perform quantum logic operations on a single qubit, be it electron, nucleus, or the whole atom. An external magnetic field is very easy to

apply to a system. After a time interval, one can expect all systems to be aligned with the field. In the initial state, a system does not move—does not precess. Next, we apply perpendicular fields to tip systems that would then start precessing. The energy emitted by the precessing systems should be detectable. Which systems would fit into such a scheme the best: electrons, nuclei, ions, atoms? The two most important requirements are that energies corresponding to precession be much lower than with electrons and that the decoherence time be much longer. Eqs. (2.8) yield $E \sim 1/m$, telling us that for nuclei, which are several orders of magnitude more massive than electrons, we can have radio frequency emissions, and this is something than can be handled easily (the proton Larmor frequency, ν, for a 1-Tesla magnetic field is 42.578 MHz). An off-the-shelf candidate for such a scheme is nuclear magnetic resonance, especially since it also offers very long coherence times.

2.3 Liquid-State Nuclear Magnetic Resonance

Nuclear magnetic resonance (NMR) is a term denoting a "Zeeman-like" method for manipulating and measuring nuclear spins. Nuclei have spins characterized by a *nuclear spin quantum number*, I, and therefore

$$S = \hbar\sqrt{I(I+1)}, \qquad S_z = m_I\hbar, \qquad m_I = -I, \ldots, I. \tag{2.20}$$

The associated intrinsic magnetic moment is

$$\boldsymbol{\mu}_I = \frac{g_N \mu_N}{\hbar}\mathbf{S}, \qquad \mu_{jz} = g_N \mu_N m_j, \tag{2.21}$$

where $\mu_N = \frac{e\hbar}{2m_p}$ (m_p being the proton mass) and g_N is the *nuclear g factor*. Nuclear magnetic moments are usually specified by the values of their g factors, which can be positive and negative. For instance, for the proton we have $g_p = 5.5856912 \pm 0.0000022$. The neutron also has a nuclear magnetic moment, and its g factor is $g_n = -3.8260837 \pm 0.0000018$. There is no direct semiclassical interpretation of the nuclear magnetic moment for the neutron, although classical charges that sum up to a net charge of zero can have a magnetic dipole moment. The g factors differ greatly from one nuclide to another. For example, ^{17}O has $g = -0.76$, ^{93}Nb has 2.47, and ^{57}Fe has 0.18. Note that $\boldsymbol{\mu}_N$ and $\mathbf{S}$ are parallel for positive and antiparallel for negative g factors.

When we put a nucleus (coupling to electrons within an atom can be treated as a small perturbation) into a static magnetic field B, we will get energy shifts analogous to those from Eqs. (2.8) and (2.15):

$$\Delta E_I = g_N \mu_N m_I B. \tag{2.22}$$

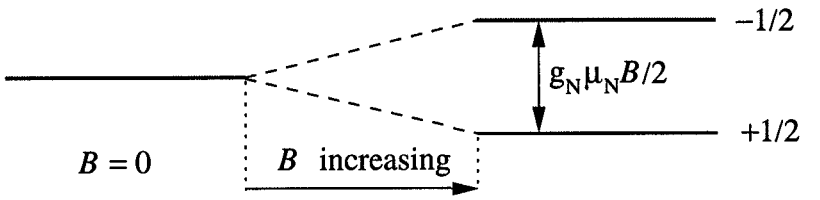

Figure 2.5. The nuclear Zeeman effect for a spin-$\frac{1}{2}$ nucleus in a magnetic field **B** for a positive nuclear g factor (for negative g, the levels are inversed).

As a result, we obtain the *nuclear Zeeman effect* shown in Fig. 2.5.

The nuclear Zeeman effect differs from its atomic version (presented in Sec. 2.2) in two respects. First, we can handle spins directly, since they are not strongly bound to another observable, unlike spin-orbit electron coupling. Second, we can directly measure ΔE_I given by Eq. (2.22), as opposed to the electron case, where we obtain a shift in a spectral line (obtained by a spontaneous transition between states determined by other observables (cf. 2.3)); actually, spontaneous transitions take place between nuclear states as well, but the probability of their occurrence as compared to the stimulated transition is negligible.

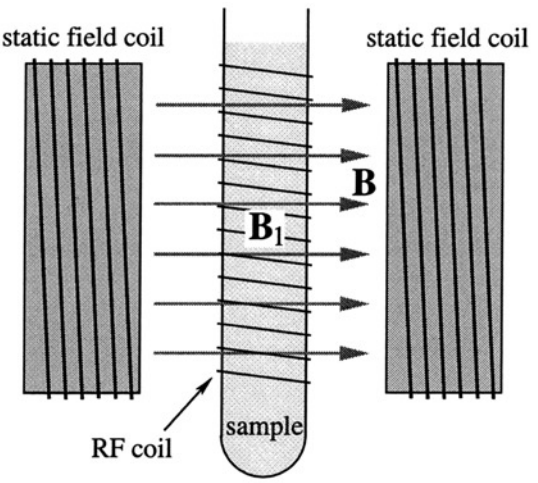

Figure 2.6. Experimental setup for NMR preparation and measurement.

By means of the device shown schematically in Fig. 2.6, we can handle nuclear spins (within a sample containing, for instance, chloroform, alanine, or trichloroethylene) using a weak rotating magnetic field $\mathbf{B}_1$ and a strong static field **B** (typically $\mathbf{B}_1 < 0.001\mathbf{B}$). In real experiments,

one does not use a rotating field but an oscillating field generated by an alternating *radio-frequency (RF)* current passing through an *RF coil.* An oscillating field is a superposition of two oppositely rotating fields.

To better understand how this process works, let us first assume that the magnetic moment $\boldsymbol{\mu}_I$—corresponding to qubit $|0\rangle$—is oriented along the z-axis. Then we briefly apply $\mathbf{B}_1$ along the x-axis to the magnetic moment and tip it a little off the z-axis. Due to the field $\mathbf{B}$, it starts precessing with frequency

$$\omega_I = \boldsymbol{\mu}_I \cdot \mathbf{B} = \frac{g_N \mu_N}{2\hbar} B, \tag{2.23}$$

where $1/2$ stands for $|m_I| = 1/2$. We continue to apply $\mathbf{B}_1$ in pulses at the frequency ω_I. We call these pulses *resonant pulses.* In the frame rotating around the z-axis at the frequency ω_I, the field $\mathbf{B}_1$ looks like a constant vector, for example, along the x-axis as shown in Fig. 2.7.

When $\boldsymbol{\mu}_I$ is tipped to the xy-plane (see Fig. 2.7 (a); we have to keep the *RF generator* on for time $t = \frac{\pi}{2\omega_I}$), the precession in the xy-plane induces an RF signal in a pickup coil (see Fig. 2.7(b); it can be a separate coil as shown here or the same coil that produces $\mathbf{B}_1$, as in Fig. 2.6).

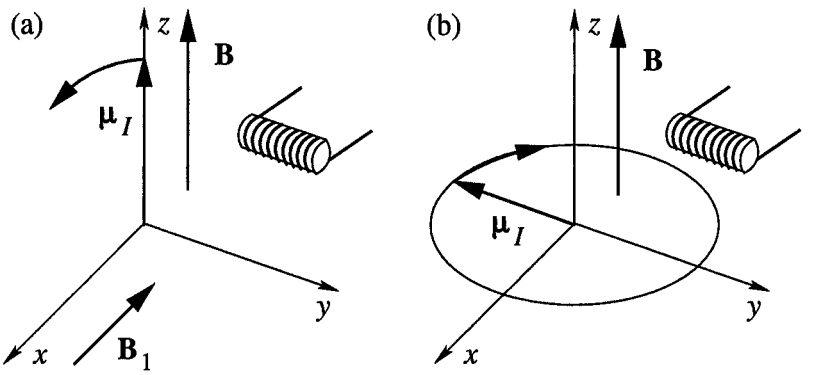

Figure 2.7. In a rotating frame, $\mathbf{B}_1$ is aligned with the x-axis and tips $\boldsymbol{\mu}_I$ into xy-plane. Then the *precession* about the z-axis induces a signal in the coil.

The signal induced by a single nucleus would be too weak and could not be measured. Consequently, we use liquid samples (usually called *lattices*). Each molecule in such a large ensemble of molecules is simultaneously placed in an initial state and subsequently subjected to RF pulses. In the end, these all induce RF signals in a *pickup coil* that sum up to a detectable output.

Different nuclei have different resonant frequencies because they have different g factors, g_N. Hence an NMR experiment can prepare and

detect states of different nuclei, i.e., different qubits. These different qubits must be coupled, and for this purpose appropriate molecules are chosen. We have already mentioned some of them above. For instance, trichloroethylene,

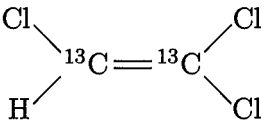

,

can incorporate three qubits: the spin-$\frac{1}{2}$ proton, H; and two spin-$\frac{1}{2}$ ^{13}C carbons (the usual ^{12}C ethylene carbons have spin 0) [Laflamme et al., 2002].

The qubits correspond to the $-\frac{1}{2}$ and $+\frac{1}{2}$ energy levels shown in Fig. 2.5 and therefore to magnetic moments that point up and down respectively:

$$|\psi_t\rangle = e^{-i\omega t/2}\alpha|0\rangle + e^{i\omega t/2}\beta|1\rangle, \tag{2.24}$$

where ω is the precession frequency given by Eq. (2.23). For the above trichloroethylene at $B = 11.7$ T, the precession frequency for protons (i.e., for H) is about 500 MHz and about 124.5 MHz and 125.5 MHz for the two ^{13}C frequencies.

By means of σ_z (given by Eq. (1.88)) aligned with the field B, we can write Eq. (2.24) as

$$|\psi_t\rangle = e^{i\omega\sigma_z t/2}|\psi_0\rangle. \tag{2.25}$$

The equation can be verified with the help of MatrixExp [cf. Eq. (1.108)]. The observable σ_z measures the spin along the z-axis. Analogously, σ_x and σ_y measure the spin along the x and y axes determined by the orthogonal weak fields $\mathbf{B}_1$ and $\mathbf{B}_2$ produced by RF coils (see Fig. 2.6, p. 95). Hence, $|\psi_t\rangle$ is the function $|\Psi\rangle$ given by Eq. (1.113), which represents a state on the Bloch sphere. The corresponding density matrix is given by Eq. (1.112), which can also be expressed as Eq. (1.92), where $\mathbf{r}$, given by Eq. (1.111), points to the states on the Bloch sphere.

Thus, one-qubit gates are rotations within the Bloch sphere implemented by RF pulses. This is described by the Hamiltonian

$$H = \frac{1}{2}(\omega_x\sigma_x + \omega_y\sigma_y + \omega_z\sigma_z), \tag{2.26}$$

and the corresponding state is

$$|\psi_t\rangle = e^{-iHt}|\psi_0\rangle. \tag{2.27}$$

For instance, by applying an RF pulse along the x-axis with duration $t = \pi/(2\omega_x)$, we get $\sqrt{\text{NOT}}$ up to a phase (cf. Eq. (1.56))

$$e^{-i\pi\sigma_x/4} = \text{MatrixExp}[-\frac{i\pi\sigma_x}{4}] = \frac{1}{\sqrt{2}}\begin{bmatrix} 1 & i \\ i & 1 \end{bmatrix}. \tag{2.28}$$

Similarly, we can get the Hadamard gate (Eq. (1.59)) up to a phase $\pi/2$:

$$e^{-i\pi\sigma_x/2}e^{-i\pi\sigma_y/4} = \frac{i}{\sqrt{2}}\begin{bmatrix} 1 & 1 \\ 1 & -1 \end{bmatrix}. \tag{2.29}$$

With the help of single qubit gates and CNOT gates, we can implement almost any gate and algorithm (see Sec. 1.19, p. 51; and Theorem 1.3, p. 53). Therefore, what is left to be considered are two gates manipulated so as to give a CNOT gate. To be able to form a CNOT gate, two gates must be coupled—the so-called *J-coupling* in NMR. J-coupling is essentially a spin–spin magnetic interaction, although distorted by its electron mediation and the molecule motion. It can be approximated by the Hamiltonian

$$H_J = \frac{\pi J}{2}\sigma_{1z}\sigma_{2z}, \tag{2.30}$$

where σ_i, $i = 1, 2$, are the Pauli operators of the nuclei and J is the *coupling constant.* J is about 100 Hz between the two ^{13}C atoms and about 100 Hz between H and the adjoining ^{13}C atoms in trichloroethylene.

J-coupling causes an increase in the precession frequency of one of the spins when the other is oriented along the $+z$-axis ($|0\rangle$ state), and a decrease when the latter spin is oriented along the $-z$-axis ($|1\rangle$ state). As a result, the former spin rotates anticlockwise in the rotating xy-plane when the latter is in the state $|0\rangle$, and clockwise when it is in the state $|1\rangle$, as shown in Fig. 2.8 (a3) and (b3).

Actually, virtually all basic quantum gates and algorithms have been implemented in NMR devices, including Shor's algorithm for factoring numbers (the number 15 was factored by means of a 7-qubit molecule [Vandersypen et al., 2001]). We can say that NMR devices, on which dozens of experiments have been carried out so far, are the first fully operating quantum computers. They are also well ahead of any other existing model and therefore deserve special attention. Yet these devices are apparently not prototypes for realistic would-be quantum computers, since we can hardly scale them up to a large enough number of qubits to produce machines of any useful size.[1] The first problem is, of course,

[1] It has been estimated that we would need a 1000-qubit quantum computer to outperform a classical computer [Preskill, 1998].

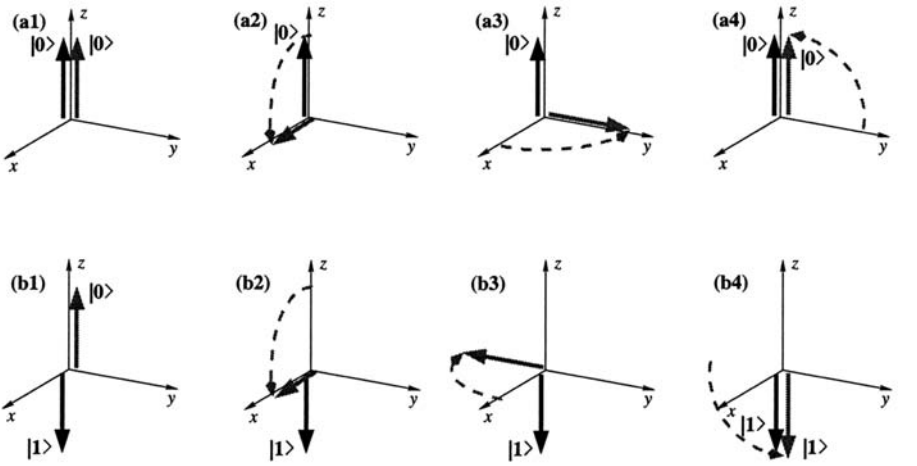

Figure 2.8. CNOT NMR gate. The a-row shows CNOT$|0\rangle|0\rangle=|0\rangle|0\rangle$ and the b-row shows CNOT$|1\rangle|0\rangle=|1\rangle|1\rangle$. The black arrow is a control qubit, and the gray arrow is a target qubit. We arrive at (a2) and (b2) by y-rotation (RF pulses). (a3) and (b3) are the consequences of the J-coupling. After applying x-rotations, we arrive at (a4) and (b4). The figure is according to Fig. 11 of [Laflamme et al., 2002].

the size of the molecules. Another problem is the operating temperature and the strength of the magnetic field, because at higher temperatures, the more qubits we have, the exponentially bigger the error. For low temperatures, Eq. (2.22) and basic thermodynamics yield $\mu_I B \sim kT$. But the strongest available NMR field today (less than 30 Tesla) corresponds to $T \approx 0.04$ K, and at this temperature the sample cannot be in the liquid state. There are many other problems with scaling, such as increasing the frequencies and decoherence. Nuclear spin quantum computer models and experiments must therefore be scaled in a different way, for example, by using a solid state, as we describe in the next section. There might also be a fundamental problem with the present implementations of NMR computing: it is not obvious whether entanglement, which can be obtained in principle, is also obtainable in realistic implementations where apparently all room-temperature thermal states should be separable [Braunstein et al., 1999].

2.4 Silicon-Based Nuclear Spins

The scalability problem that NMR quantum computers have with the size of molecules stems from the fact that we address nuclei by their chemical identity. We do so with the help of RF coils tuned to the resonant frequencies characteristic of the addressed nuclei. This is

apparently simply not feasible for molecules with more than 20 qubits. Hence, it would be very convenient if we could find a way to address nuclei by their addresses as in classical computers. It would be even more convenient if we could take advantage of the existing research on the materials used by the standard computer industry, which currently approaches the quantum realm from the "other side." And this is exactly what recent silicon-based nuclear spin computer models offer.

Nuclear spins in solid state materials interact with electron spins in a way similar to that in which electron angular momenta interact with electron spins through the spin–orbit interaction (Eq. (2.10) and Fig. 2.3), i.e., the nuclear magnetic moment interacts with the electron magnetic moment. This interaction—called the *hyperfine interaction*—contributes to the Hamiltonian of the whole system containing nuclei and electrons with the term

$$H_h = A\,\mathbf{I}\cdot\mathbf{S}, \tag{2.31}$$

where $\mathbf{S}$ and $\mathbf{I}$ are the electron and nuclear spins, respectively (cf. Sec. 2.3, p. 94).

With $S = \frac{1}{2}$ and $I = \frac{1}{2}$, the base states for the nucleus and the electron taking part in the hyperfine interaction are $|\uparrow\rangle_e|\uparrow\rangle_N$, $|\uparrow\rangle_e|\downarrow\rangle_N$, $|\downarrow\rangle_e|\uparrow\rangle_N$, and $|\downarrow\rangle_e|\downarrow\rangle_N$. Their arbitrary state is therefore

$$|\Psi\rangle = C_1|\uparrow\rangle_e|\uparrow\rangle_N + C_2|\uparrow\rangle_e|\downarrow\rangle_N + C_3|\downarrow\rangle_e|\uparrow\rangle_N + C_4|\downarrow\rangle_e|\downarrow\rangle_N. \tag{2.32}$$

The action of the spin operators on the base states is the standard Pauli matrix action on them. For example, $S_y|\uparrow\rangle_e|\downarrow\rangle_N = \sigma_y^e|\uparrow\rangle_e|\downarrow\rangle_N = i|\downarrow\rangle_e|\downarrow\rangle_N$, $I_x|\uparrow\rangle_e|\downarrow\rangle_N = \sigma_x^N|\uparrow\rangle_e|\downarrow\rangle_N = |\uparrow\rangle_e|\uparrow\rangle_N$, and $S_xI_z|\uparrow\rangle_e|\downarrow\rangle_N = \sigma_x^e\sigma_z^N|\downarrow\rangle_e|\uparrow\rangle_N = -|\downarrow\rangle_e|\downarrow\rangle_N$. The total Hamiltonian is a constant plus the interaction part given by Eq. (2.31):

$$H = E_0\mathbb{1} + A\,\boldsymbol{\sigma}^e\cdot\boldsymbol{\sigma}^N. \tag{2.33}$$

Using Eq. (2.6) and (2.21), we can also understand this interaction as the interaction of two magnetic dipoles whose energy depends on $\boldsymbol{\mu}_S\cdot\boldsymbol{\mu}_I$. The difference between the classical and quantum dipole interactions is that the classical interaction depends on the distance between the dipoles, while the quantum interaction does not—the Hamiltonian (2.33) gives only the average interaction energy [Feynman et al., 1965, 12-5]. And this is the key point for our application because in the solid state, in particular in semiconductors, the electron wave function is spread through the crystal lattice surrounding a nucleus or ensemble of nuclei.

Resolving $|\Psi\rangle$ into base states, considering its time evolution, and taking into account that $C_i = C_i(t) = \langle\Psi_i(t)|\Psi(t)\rangle = \langle\Psi_i|\Psi\rangle$, $i = 1,\ldots,4$,

where $|\Psi_i\rangle$ is one of the four base states from Eq. (2.32), we get [Feynman et al., 1965, 8-9]

$$i\hbar\frac{dC_i}{dt} = \sum_{j=1}^{4} H_{ij}C_j, \qquad i = 1, \ldots, 4, \tag{2.34}$$

where $H_{ij} = \langle i|H|j\rangle$. We obtain these elements by applying H to all base states. For instance,

$$H|\uparrow\uparrow\rangle = A\,\boldsymbol{\sigma}^e\cdot\boldsymbol{\sigma}^N = A(\sigma_x^e\sigma_x^N + \sigma_y^e\sigma_y^N + \sigma_z^e\sigma_z^N)|\uparrow\uparrow\rangle = A\,|\uparrow\uparrow\rangle, \ldots,$$

where we adopt the notation $|\uparrow\uparrow\rangle$ for $|\uparrow\rangle_e|\uparrow\rangle_N$, etc. This yields

$$H_{11} = \langle\uparrow\uparrow|H|\uparrow\uparrow\rangle = A, \quad H_{12} = \langle\uparrow\downarrow|H|\uparrow\uparrow\rangle = 0, \ldots, \tag{2.35}$$

and taking

$$C_i = a_i e^{-i\omega t} \tag{2.36}$$

we get the following system:

$$\begin{aligned} Ea_1 &= Aa_1, & Ea_2 &= -Aa_2 + 2Aa_3, \\ Ea_3 &= Aa_2 - 2Aa_3, & Ea_4 &= Aa_4. \end{aligned} \tag{2.37}$$

From the first and the fourth equations, we get the following energies and states:

$$E_I = A, \quad |I\rangle = |\uparrow\uparrow\rangle, \quad E_{II} = A, \quad |II\rangle = |\downarrow\downarrow\rangle, \tag{2.38}$$

and from the second and the third we get

$$\begin{aligned} E_{III} &= A, & |III\rangle &= \frac{1}{\sqrt{2}}\left(|\uparrow\downarrow\rangle + |\downarrow\uparrow\rangle\right), \\ E_{IV} &= -3A, & |IV\rangle &= \frac{1}{\sqrt{2}}\left(|\uparrow\downarrow\rangle - |\downarrow\uparrow\rangle\right). \end{aligned} \tag{2.39}$$

Hence, the states $|I\rangle$, $|II\rangle$, and $|III\rangle$ are degenerate, and a transition from them to the state $|IV\rangle$ causes an emission of a microwave quantum, $\Delta E = 4A = \hbar\omega$. Of course, the atom would also absorb a quantum of the frequency ω.

When we put the atom into an external magnetic field $\mathbf{B}$, the upper line splits. Let us look at the details, following [Feynman et al., 1965, 12-9]. Feynman presented the calculations only for hydrogen, but they approximate any atom with nuclear spin $\frac{1}{2}$ and a single electron in the outer shell [Kane, 2000]. The Hamiltonian is

$$H = A\,\boldsymbol{\sigma}^e\cdot\boldsymbol{\sigma}^N + g_S\mu_B\boldsymbol{\sigma}^e\cdot\mathbf{B} - g_N\mu_N\boldsymbol{\sigma}^e\cdot\mathbf{B}, \tag{2.40}$$

where g_N, μ_N, and $g_S\mu_B$ are given by Eqs. (2.6) and (2.21). Proceeding in the same way as above and obtaining equations analogous to Eqs. (2.35)–(2.37), we get the following energies:

$$\begin{aligned} E_I &= A + (g_S\mu_B - g_N\mu_N)B, \\ E_{II} &= A - (g_S\mu_B - g_N\mu_N)B, \\ E_{III} &= A\,(-1 + 2\sqrt{1 + (g_S\mu_B + g_N\mu_N)^2B^2/4A^2}\,), \\ E_{IV} &= -A\,(1 + 2\sqrt{1 + (g_S\mu_B + g_N\mu_N)^2B^2/4A^2}\,). \end{aligned} \tag{2.41}$$

Since $g_S\mu_B$ (for the electron) is about thousand times larger than $g_N\mu_N B$ (for the nucleus), we get the plot shown in Fig. 2.9.

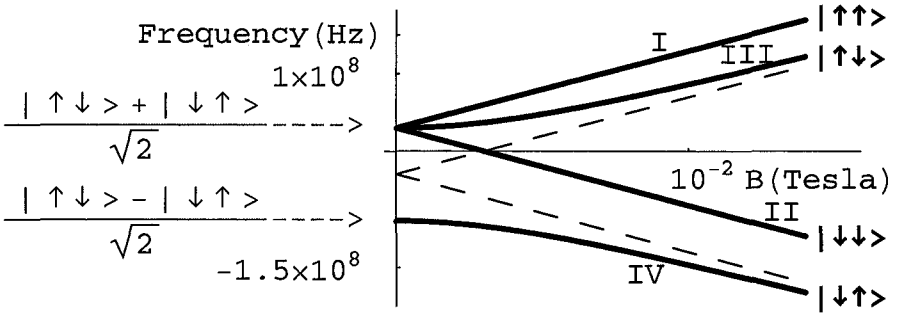

Figure 2.9. The energy levels (Eqs. (2.41)) and states of an atom with a nucleus of spin $\frac{1}{2}$ and a single electron in the highest shell with a negligible spin-orbit interaction. The dashed lines are $-A+(g_S\mu_B+g_N\mu_N)B$ and $-A-(g_S\mu_B+g_N\mu_N)B$. All emission and absorption transitions are allowed.

From Eq. (2.41) we can see that for large B, the dashed linear functions given in Fig. 2.9 approximate E_{III} and E_{IV}. Thus, we obtain four linear functions representing four energies and four different states $|I\rangle = |\uparrow\uparrow\rangle$, $|II\rangle = |\downarrow\downarrow\rangle$, $|III\rangle = C_{III2}|\uparrow\downarrow\rangle + C_{III3}|\downarrow\uparrow\rangle$, and $|IV\rangle = C_{IV2}|\downarrow\uparrow\rangle - C_{IV3}|\downarrow\uparrow\rangle$, where C_j are (for $B > 0$ and Hamiltonian (2.40)) determined by analogy with Eq. (2.34). It is straightforward to show [Feynman et al., 1965] that for small magnetic fields, C_{III2}=C_{III3}=C_{IV2}=C_{IV3}=$1/\sqrt{2}$ and for large ones, $C_{III2} = 1$, $C_{III3} \approx 0$, $C_{IV2} \approx 0$, and $C_{IV3} = 1$.

These properties of atoms with nuclear spin $\frac{1}{2}$, which have no orbital degree of freedom and have a single electron in the highest shell with a negligible spin–orbit interaction, promise comparatively easy handling within a solid state environment. The natural candidate for the atom is phosphorus, which appears in only one isotope ^{31}P in nature, and

therefore is 100% pure. It has one outer electron, and $I = \frac{1}{2}$. The natural solid state candidate is the group IV of Si semiconductors with $I = 0$. Current intensive efforts to shrink silicon processors may yield many techniques that might prove helpful for implementation of qubits into an Si semiconductor environment. Recently Bruce Kane proposed such an implementation [Kane, 1998; Kane, 2000; Skinner et al., 2003]. Let us consider the details.

The Si substrate is an insulator at temperatures under 1 K, i.e., there are no free electrons. Phosphorus atoms can be introduced as donors in controllable positions in the substrate. As we have pointed out above, the energy levels of the hyperfine interaction between the electron and nuclear spins in ^{31}P are well defined, and the transitions between the levels shown in Fig. 2.9 are induced by a globally applied radio frequency magnetic field B_{RF}. Bringing the systems into resonance with B_{RF} is done by *A-gates* as shown in Fig. 2.10.

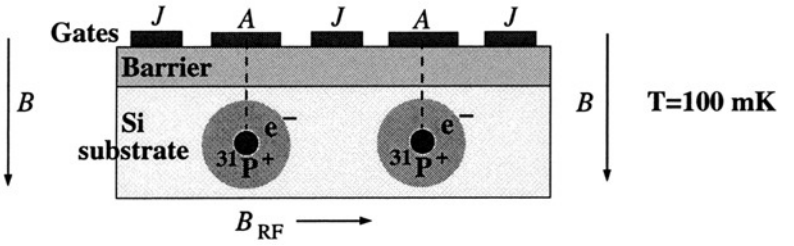

Figure 2.10. Phosphorus donors in an Si substrate. *A*-gates control the nuclear-resonance frequency, and *J*-gates control the electron-mediated coupling between the nuclear spins. The figure is according to Fig. 1 of [Kane, 1998].

A-gates are small electrodes with the help of which one can address qubits in the following way. In contrast with NMR, where each qubit has a different chemical identity and therefore a different Larmor resonance frequency, the process of addressing the nuclei by means of the external *RF field* can be carried out by only a single frequency, because all qubits have the same chemical identity (^{31}P) and all see the same chemical environment (silicon). Hence, we cannot set the external RF field B_{RF} to this frequency because it would tip the spins of all qubits indiscriminately. The solution is to apply a slightly detuned external B_{RF} and to tune in a chosen qubit instead of the field itself. We do so by means of the *A*-gate voltage over the chosen nucleus. It draws the electron off the nucleus, as shown in Fig. 2.11, thereby changing the resonant frequency of the nucleus so as to coincide with that of the external fields B_{RF}.

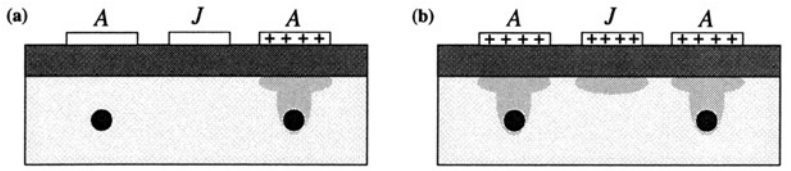

Figure 2.11. (a) One qubit operation: A-gate bias brings the nuclear spin into resonance with external RF field; (b) Two-qubit operation: a positive voltage bias applied to the J-gate lowers the potential barrier between donor sites and turns on exchange electron-mediated coupling between the nuclei.

Two nuclear spins from two adjacent ^{31}P atoms can interact with the same electron and therefore be coupled through an electron mediation. Such an electron-mediated interaction can therefore be controlled by voltages applied to metallic gates above the Si substrate. In Fig. 2.10, this is done by *J-gates*. At sufficiently low temperatures (about 1 K), the electron spin relaxation time is over 15 minutes and the nuclear spin relaxation is over 10 hours, so that there is no problem with decoherence. With even lower temperatures, arbitrarily long relaxation times can be achieved.

For a computation, we can use nuclear spins as memory and electron spins as mediators of interaction between the nuclear spins. There are several reasons for taking this approach. The relaxation time of nuclear spins is much longer, they have no orbital degrees of freedom, and they rotate much more slowly in the external magnetic field B than electrons.

The Hamiltonian of two coupled nucleus–electron systems is

$$H = H_B + A_1\,\boldsymbol{\sigma}^{1e}\cdot\boldsymbol{\sigma}^{1N} + A_2\,\boldsymbol{\sigma}^{2e}\cdot\boldsymbol{\sigma}^{2N} + J\,\boldsymbol{\sigma}^{1e}\cdot\boldsymbol{\sigma}^{2e}, \tag{2.42}$$

where H_B is the part containing the magnetic field interaction terms as in Eq. (2.40); A_1, A_2 are the hyperfine interaction energies; and J is the exchange energy, depending on the degree to which the electron wave function overlaps. The second and third terms in the Hamiltonian H above are called the H_A part [Kane, 1998; Kane, 2000]. The H_B part is also called the *Zeeman magnetic* part [Levy, 2002]. Again, as with Eq. (2.41), we can use the calculations for the hydrogen [Kane, 2000] to get

$$J(r) \sim E_b \left(\frac{r}{a_B}\right)^{\frac{5}{2}} \exp\left(-\frac{2r}{a_B}\right), \tag{2.43}$$

where r is the distance between the donors and a_B is the semiconductor Bohr radius. J can be varied by electrostatic potentials imposed by J-gates positioned between donors, as shown in Figs. 2.10 and 2.11.

We should emphasize that the H_B part in Eq. (2.42) contains terms that involve a strong external field B (which should be called B_z, but it is usual in the literature to simply denote it B),

$$-g_N\mu_N B_z(\sigma_{1N}^z + \sigma_{2N}^z) + g_S\mu_B B_z(\sigma_{1e}^z + \sigma_{2e}^z), \tag{2.44}$$

and an oscillating field B_{RF} (often also denoted B_{ac}), which is positioned in the xy-plane)

$$\begin{aligned} &B_{\text{RF0}}(t)\cos\omega t[-g_N\mu_N(\sigma_{1N}^x + \sigma_{2N}^x) + g_S\mu_B(\sigma_{1e}^x + \sigma_{2e}^x)] \\ &+B_{\text{RF0}}(t)\sin\omega t[-g_N\mu_N(\sigma_{1N}^y + \sigma_{2N}^y) + g_S\mu_B(\sigma_{1e}^y + \sigma_{2e}^y)]. \end{aligned} \tag{2.45}$$

A negative voltage bias applied to the J-gate decouples the adjacent spins, and a positive voltage couples them. A positive voltage bias applied to the A-gate draws the electron away from the nucleus, thus reducing the interaction between the electron and nuclear spins and therefore the energy difference between $|\uparrow\rangle_N$ and $|\downarrow\rangle_N$. This outcome allows us to make an arbitrary transition between these states by achieving a resonance with a global RF oscillating magnetic field B_{RF}. Actually, by applying an appropriate voltage fluctuation to A-gates we can rotate—similarly to the NMR rotations presented in Sec. 2.3—the qubits (nuclear spins) and thus change the levels and states (see Fig. 2.9, p. 102). This suffices for handling individual qubits as well as controlled operations. For example, the CNOT of the electron spin, conditioned on the state of the nuclear spin [Kane, 2000], can be achieved by exciting the transition between the lower two states (see Fig. 2.9, p. 102) with the radio frequency magnetic field B_{RF}, provided that the field B is strong enough: $(|\downarrow\rangle_e|\uparrow\rangle_N) \leftrightarrow |\uparrow\rangle_e|\uparrow\rangle_N$. However, if we want to scale up the number of qubits then we have to choose a different approach. But let us first say a few words about reading off the results of a computation.

To read out the states of qubits in which a finished calculation leaves them, we use—unlike NMR computers—charge measurements. Measurements of the magnetic fields of electrons and nuclei would also be a possibility, but these are much slower than the charge measurements. Single charge measurements can be carried out by a *single electron transistor*, SET, in microseconds as we mentioned in Sec. 1.5 (p. 12). Here is yet another example of how recent advances in the shrinking of classical computers can help us in building a solid state quantum computer.

Measurements of nuclear spins are made by *charge measurements*[2] of electrons for the exchange energy $J > \mu_B B/2$. (Computations are made

[2]The SETs are positioned above atoms and the charge motion within Si substrate (see Fig. 2.13) change the potential of a SET part called *island*. This changes SET's conductance and enables measurements.

for $J < \mu_B B/2$ because for lower J, the electrons are fully polarized, while for $J > \mu_B B/2$, the energy levels are split (cf. Fig. 2.9, p. 102). Then the state $(|\uparrow\rangle_{1e}|\downarrow\rangle_{2e} - |\downarrow\rangle_{1e}|\uparrow\rangle_{2e})/\sqrt{2}$ has the lowest energy and $|\uparrow\rangle_{1e}|\uparrow\rangle_{2e}$ has the next to lowest. These two states are coupled to the nuclear spin states, which then determine whether the electrons will be in the state $|\uparrow\rangle_{1e}|\uparrow\rangle_{2e}$ or in $(|\uparrow\rangle_{1e}|\downarrow\rangle_{2e} - |\downarrow\rangle_{1e}|\uparrow\rangle_{2e})/\sqrt{2}$. Since the charge measurement can differentiate between these two electron states, we can infer the values of the nuclear spin states. Thus we can recover both electron spin and nuclear spin. At the same time, this outcome defines the qubits we can work with. The qubits are given by [Kane, 2000]

$$|0\rangle \equiv |\uparrow\rangle_e|\downarrow\rangle_N + |\downarrow\rangle_e|\uparrow\rangle_N, \qquad |1\rangle \equiv |\uparrow\rangle_e|\downarrow\rangle_N - |\downarrow\rangle_e|\uparrow\rangle_N. \tag{2.46}$$

Two-qubit systems and the operations (gates) one can carry out on them are determined by the Hamiltonian given by Eqs. (2.42), (2.44), and (2.44). The calculations of the energy levels for a two-qubit system are straightforward although tedious. They can be done in the same way that the calculations for the one-qubit system, described by Hamiltonian (2.40), were carried out above. Thus, we get equations analogous to Eq. (2.41), and we get Fig. 2.12, which corresponds to Fig. 2.9 (p. 102).

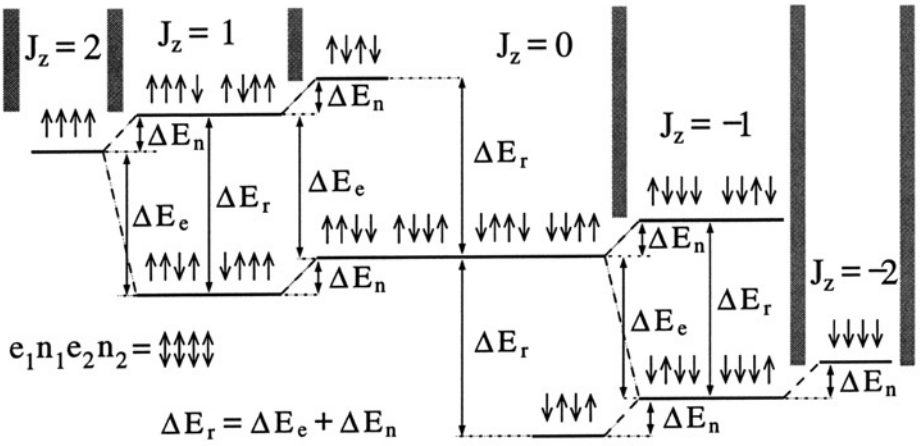

Figure 2.12. Magnetic energy levels of the total spin subspaces of the two-qubit Kane computer. Flipping the electron or nuclear spin changes the energy by ΔE_e or ΔE_N, respectively. Flipping both of them changes the energy by ΔE_r [Skinner et al., 2003].

Now, in order to carry out, for example, the CNOT operation

$$\begin{aligned}\mathrm{CNOT}|1\rangle_1|0\rangle_2 &= \mathrm{CNOT}(|\uparrow\rangle_{1e}|\downarrow\rangle_{1N} - |\downarrow\rangle_{1e}|\uparrow\rangle_{1N}) \\ &\qquad (|\uparrow\rangle_{2e}|\downarrow\rangle_{2N} + |\downarrow\rangle_{2e}|\uparrow\rangle_{2N}) \\ &= (|\uparrow\rangle_{1e}|\downarrow\rangle_{1N} - |\downarrow\rangle_{1e}|\uparrow\rangle_{1N})(|\uparrow\rangle_{2e}|\downarrow\rangle_{2N} - |\downarrow\rangle_{2e}|\uparrow\rangle_{2N}) \\ &= |1\rangle_1|1\rangle_2, \end{aligned} \tag{2.47}$$

we have to find a function that will change the phase of $|\downarrow\rangle_{2e}|\uparrow\rangle_{2N}$ depending on the phase of $|\downarrow\rangle_{1e}|\uparrow\rangle_{1N}$. We do this by allowing electrons to act on the nucleus from the other qubit by means of the hyperfine interaction. Kane designed a hyperfine evolution for this purpose [Skinner et al., 2003].

The idea is to apply *bit trains* of voltage pulses applied to A-gates while *S-gates* shuttle electrons from and to donors. (S-gates correspond to the J-gates in Figs. 2.10 and 2.11.)

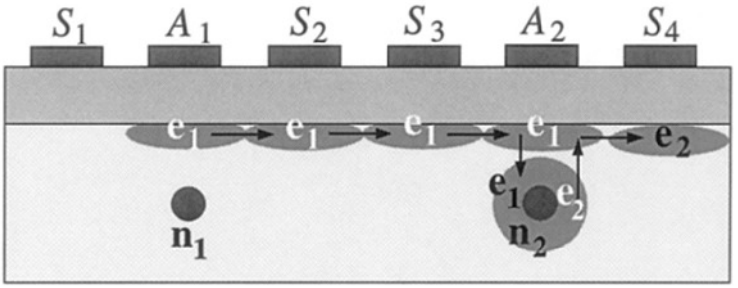

Figure 2.13. Entangling electron-nucleus qubits e_1N_1 and e_2N_2. S-gates displace e_2 and shuttle e_1 from N_1 to N_1. A-gates draw electrons away from nuclei and change their states enough for the global RF field B_{RF} to flip targeted sub-states [Skinner et al., 2003].

First, we apply a positive voltage to A-gate A_2 to draw the electron e_2 off the donor ^{31}P atom, and then, by applying a positive voltage to S-gate S_4, we move e_2 aside. Next we shuttle electron e_1 to n_2 in order for A-gate S_2 above n_2 to apply hyperfine interaction, as shown in Fig. 2.13. Through this interaction, the two qubits become entangled. We would like to have pure hyperfine evolution according to the H_A part of Eq. (2.42); however, the magnetic field (the H_B part of Eq. (2.42)), whose role is to augment the interaction, is on all the time. The H_A part should now contain terms that describe the entanglements, in particular $\boldsymbol{\sigma}^{1e}\cdot\boldsymbol{\sigma}^{2N}$ and $\boldsymbol{\sigma}^{2e}\cdot\boldsymbol{\sigma}^{1N}$:

$$H_A = \sum_{i,j} A_{ij}\boldsymbol{\sigma}^{ie}\cdot\boldsymbol{\sigma}^{jN}. \tag{2.48}$$

We can achieve this outcome by "slicing" the time needed for the hyperfine evolution into many steps using the Trotter formula [Skinner et al., 2003; Nielsen and Chuang, 2000]:

$$e^{-iH_A/\hbar} \approx \left[e^{iH_B\Delta t/2\hbar}e^{-i(H_A+H_B)\Delta t/\hbar}e^{iH_B\Delta t/2\hbar}\right]^a. \tag{2.49}$$

In this way we apply the full Hamiltonian evolution and still have only H_A, i.e., pure hyperfine evolution. To apply this result, we take the number a of $\Delta t = t/a$ steps. The middle term on the right-hand side of Eq. (2.49) corresponds to the full Hamiltonian evolution and the two other terms correspond to a magnetic interaction that corrects the magnetic evolution. The full period of the hyperfine interaction is given as $T_B = h/\Delta E_r$ (see Fig. 2.12). The hyperfine period is $T_A = h/4A$.

Using digital bit trains that apply voltage pulses to A-gates, we can construct arbitrary quantum logic gates with the help of ϕ pulses of magnetic evolution, (B, ϕ), and θ pulses of pure hyperfine evolution, (A, θ), where

$$(B, \phi) \equiv e^{-iH_B\phi T_B/h}, \qquad (A, \theta) \equiv e^{-iH_A\theta T_A/h}. \tag{2.50}$$

For instance, CNOT can be implemented as follows:

$$\text{CNOT} = M\,N\,M^\dagger, \tag{2.51}$$

where M contains only single qubit operations

$$M = \left(B, \frac{3\pi}{2}\right)(A_{11} + A_{22}, \pi)\left(A_{11}, \frac{\pi}{2}\right)\left(B, \frac{\pi}{2}\right),$$

and N contains only mixed qubit operations that stem from the entanglement

$$N = \left(A_{12} + A_{21}, \frac{3\pi}{2}\right)\left(B, \frac{\pi}{2}\right)(A_{21}, \pi)\left(B, \frac{3\pi}{2}\right)\left(A_{12} + A_{21}, \frac{\pi}{2}\right).$$

This outcome could be simplified if we used two different g factors, g_1 and g_2 [Levy, 2002] (neighboring ^{31}P's could be embedded into different surrounding substrates). But for the time being, this result, is only a theoretical, because placing ^{31}P's into just one medium—that would be pure enough—and into precisely defined locations is already an extremely demanding task.

Stressing that the Kane computer—as we have seen above—satisfies the five requirements for the implementation of quantum computation given in Sec. 2.6, we can conclude that the Kane computer is a promising technological candidate for a would-be quantum computer. Although

the challenges facing a realization of this project are tremendous, it is expected that the current advances in "shrinking" conventional silicon electronics will inevitably lead to applicable new solutions [Clark et al., 2003; Schenkel et al., 2003].

2.5 Ion Traps

Another promising candidate for a possible would-be quantum computer makes use of cold trapped ions [Cirac and Zoller, 1995]. In the last ten years, experiments with trapped ions have yielded results competitive with those achieved on NMR setups. Besides, these experiments can be modified so as to enable scalability [Cirac and Zoller, 2000; Cirac and Zoller, 2004]. Realistic implementations of quantum calculation with ions face tremendous problems, but the physics behind the process has been worked out more completely than the physics of the Kane computer, where there are still unanswered questions.

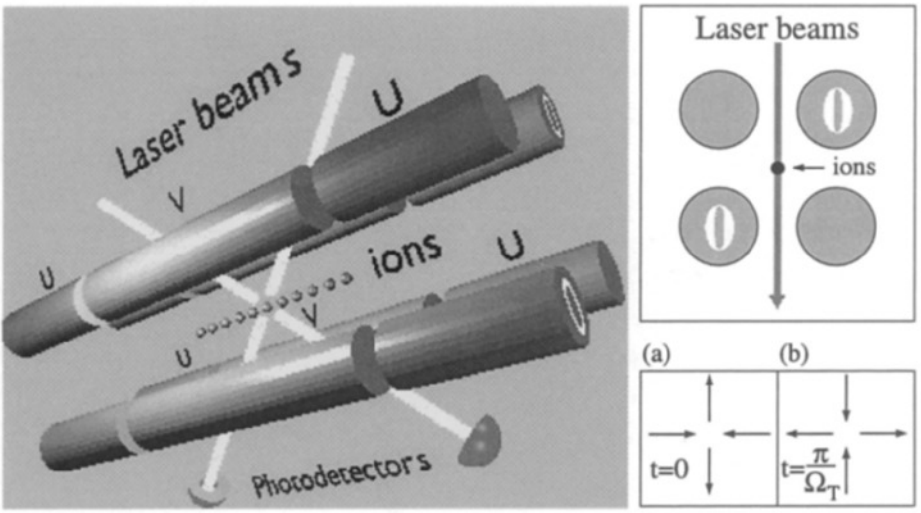

Figure 2.14. A possible ion trap realization for a large number of ions: Paul's linear trap (not to scale) [Cirac and Zoller, 1995; Steane, 1997]. The opposite end sections of two of the rods are under static positive voltage U to force the ions to stay at a constant average distance from each other. An AC voltage $V = V_0 \cos(\Omega_T t)$ is applied to the middle parts of these rods. The other two rods are grounded (0). The insets (a) and (b) show the dynamics of the electric fields at $t = 0$ and $t = T/2$, respectively, where T is the period of the AC current.

Ion traps used in experiments are mostly Paul traps (electrical field only, as opposed to Penning traps, which use both electric and magnetic fields). To confine ions to well-localised positions in space, we must use

a time-dependent RF (see p. 96) electric field.[3] To trap large numbers of ions, we cannot use the standard spherical traps with hyperbolic fields, which have an exact solution [Demtröder, 1996, 14.2.1], because in such a trap we cannot keep all the ions in the middle of the trap where the RF field is zero. This would cause too large a motion and therefore the heating of ions.

The so-called *linear ion trap*, shown in Fig. 2.14, is used for trapping large numbers of ions. The RF field is zero along the central line of the electrode configuration. The ions are confined along this line with static electric fields: the ends of the segmented rods are held at a positive potential [Steane, 1997]; alternatively, one can have a static ring around the end sections of the AC electrodes or just have positively charged points at the each end of the ion line. Let this line be our x-axis. If the potentials are chosen appropriately, cold ions may be harmonically trapped in all three dimensions. The directions of the corresponding fields, shown in insets (a) and (b) of Fig. 2.14, determine the x- and y-axes. The displacements in the x, y-directions are much faster than in the z-direction: $\omega_z \ll \omega_x, \omega_y$. The total energy of the ions is the sum of their kinetic energy, E_k, and potential energy, E_p:

$$E_k = \sum_{i=1}^{N} \frac{p_{ix}^2 + p_{iy}^2 + p_{iz}^2}{2m}, \qquad E_p = \sum_{i=1}^{N} \left(\zeta z_i^n + \sum_{i>j}^{N} \frac{Q^2}{|z_i - z_j|} \right), \quad (2.52)$$

where the potential energy consists of the Coulomb repulsion between ions and a term describing trapping in the z-direction.

To get ion behavior that we can control, we have to reduce the energy in the z direction as much as possible—mathematically this means obtaining a well-behaved potential energy in Eq. (2.52), which could be approximated by the lowest terms of its Taylor series. A physical way to achieve this result is to require that the kinetic energy of an ion be much less then the quantum of energy corresponding to its vibration in the z-direction, $\hbar\omega_z$. Such vibrational quanta of energy are called *phonons*. Since thermodynamically the kinetic energy of particles corresponds to their temperature, this requirement can be expressed as $k_B T \ll \hbar\omega_z$, where k_B is the Boltzmann constant and T is the temperature; i.e., we

[3]Basic electrostatics tells us that it is not possible to design an ion trap using only static fields. More precisely, Gauss' Law (1st Maxwell's equation) tells us that in a charge-free region of space, there can be no local minimum (or maximum) in the potential. This result can also be expressed by the continuity equation: the divergence of the electric field is equal to zero—hence all the field lines going to the center of the ion trap must come out of the trap center in some other direction. Hence a positive charge cannot be confined there. This result is sometimes referred to as *Earnshaw's theorem* (Earnshaw first arrived at it in 1842).

have to cool down the ions. However, here we have an example of microscopic cooling in one dimension, while in the other two the ions oscillate rapidly ($\omega_z \ll \omega_x, \omega_y$).

Therefore, the cooling cannot be an overall thermodynamical cooling but has to be a targeted reduction of the kinetic energy of ions in a chosen direction. This reduction can be accomplished by Doppler laser cooling. The process works as follows. First, we need a near-perfect vacuum so that there are no other atoms apart from our ions that could possibly kick the ions. Then we direct laser beams along the z-axis towards ions in the trap. Only photons of a frequency that can excite an atom (ion) will interact with it. Photons of other frequencies cannot "see" the atom because they have wavelengths that are much longer than the dimensions of atoms. We also say that the atom has a much bigger cross section for the former photons. Now an atom moving towards a laser beam has higher transition frequencies than one moving away from it (Doppler effect), and if we tune the laser beam so as to match the former frequencies, the photons will kick (transfer their momentum $p = h/\lambda$ to) the atoms coming towards them and will not interact with the atoms going away from them. We also must apply so-called *Sisyphus cooling* (see p. 119) until we reach the temperature $T \ll \hbar\omega_z/k_B$.

For ions with energy reduced in this way in the z-direction (we also limit the kinetic part to the z-axis), we can expand the potential energy in Eq. (2.52) around the equilibrium position and approximate it by only the first terms of the Taylor series. We get quadratic terms (for $j = i$) and mixed terms (for $j \neq i$), but by expressing these terms with the help of normal modes of oscillation (see Fig. 2.15 (b)), we get rid of mixed terms and obtain the harmonic oscillator Hamiltonian

$$H = \sum_{i=1}^{N} \left(\frac{p_{zi}^2}{2m} + \frac{1}{2} m\omega_z^2 z_i^2 \right), \tag{2.53}$$

where H, p_{zi}, and z_i are operators, but we drop the "hats" to ease the notation. The last two operators satisfy the commutation rules:

$$[z_i, p_{zi}] = i\hbar. \tag{2.54}$$

In Sec. 1.17 (for Eq. (1.69)), we introduced the annihilation operator a and several "rules of thumb" for applying it to state vectors. Its Hermitian conjugate, $a^\dagger$, is called the *creation operator* and $N = a^\dagger a$ is the *number operator*. These names are clarified by their actions on states vectors given below.

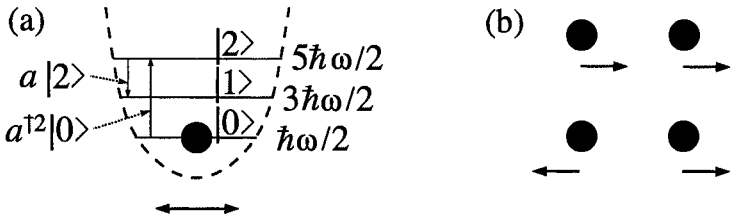

Figure 2.15. (a) Harmonic oscillator potential; (b) normal modes: the upper mode is the left-to-right motion of both ions together, i.e., the center of mass (CM) mode, and the lower one is the one in which CM does not move, the so-called *stretch mode.*

We define the *annihilation operator* for each ion as follows:

$$a = \sqrt{\frac{1}{2\hbar}}\left(\sqrt{m\omega_z}z + \frac{ip_z}{\sqrt{m\omega_z}}\right). \tag{2.55}$$

Using the corresponding creation and number operators and the commutation rule given by Eq. 2.54 we can write down the Hamiltonian (2.53) applied to its eigenstates $|n\rangle$ as

$$H|n\rangle = \frac{\hbar\omega_z}{2}(aa^\dagger + a^\dagger a)|n\rangle = \hbar\omega_z(N + \frac{1}{2})|n\rangle = E_n|n\rangle, \tag{2.56}$$

We emphasize here that $|n\rangle$ means an n-phonon state. Thus, $|0\rangle$ and $|1\rangle$ mean states containing zero and one phonons.

Note that phonons are bosons and that a and $a^\dagger$ satisfy the following anticommutation relations:

$$a_j^\dagger a_k + a_k a_j^\dagger = \delta_{jk}. \tag{2.57}$$

The names *creation* and *annihilation operators* come from the following relations one can easily derive [Messiah, 1965]:

$$a^\dagger|n\rangle = \sqrt{n+1}|n+1\rangle, \quad a|n\rangle = \sqrt{n}|n-1\rangle \quad n \neq 0, \quad a|0\rangle = 0.$$

We also obtain $N|n\rangle = n|n\rangle$, which clarifies the name number operator, as well as

$$E_0 = \frac{1}{2}\hbar\omega_z, \quad E_1 = \frac{3}{2}\hbar\omega_z, \quad \ldots \quad E_n = (n + \frac{1}{2})\hbar\omega_z, \quad \ldots, \tag{2.58}$$

shown in Fig. 2.15.

Therefore the ground state $|0\rangle$ corresponds to no phonons, i.e., to the CM motion with frequency ω_z, and has the energy $\hbar\omega_z/2$ for each phonon. The first mode corresponds to the number state 1 and to one

phonon, and since the ions are moving in opposite directions, their frequency is (cf. Fig. 2.15) $\sqrt{3}\omega_z$, etc. It can be shown that these frequencies do not change when we increase the number of ions, and this finding is important for the scalability of the setup.

To obtain qubits for computation, we combine these global, phonon states with individual states of particular ions. The latter states we obtain by applying laser beams to individual ions. These states are two-level states that we can obtain in several ways: (a) by Zeeman splitting (Sec. 2.2, 88), achieved with the help of a magnetic field applied to the ground state, (b) by the two-beam Raman scheme for resolving sublevels of a ground state of ions with hyperfine interaction, and (c) by optical transitions between fine structure states for ions with zero nuclear angular momentum, etc. The experimental realizations are too numerous [Wineland et al., 1998; Kielpinski et al., 2002; Cirac and Zoller, 2000; Cirac and Zoller, 2004] to be reviewed here. Therefore, we shall present a schematic of one of the first proposals that remains a very instructive way of combining individual and collective states [Cirac and Zoller, 1995].

Before we dwell on the proposal itself, let us first consider a semiclassical description of a laser controlling a two-level system, as shown in Fig. 2.16. The laser beam of frequency ω_L induces the transitions between the ground and excited levels of an atom. We describe the beam by the classical electromagnetic plane wave given by Eq. (1.8). The equation's real part is

$$\mathbf{E} = \mathbf{E}_0 \cos(\mathbf{k} \cdot \mathbf{r} - \omega t + \phi), \tag{2.59}$$

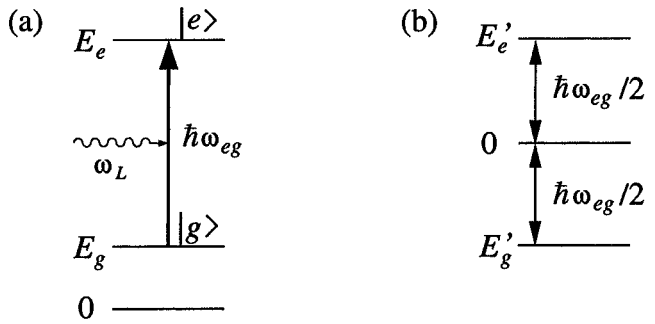

Figure 2.16. (a) A two-level system interacting with a laser beam field; (b) redefined zero-energy—see Eq. (2.87).

Since the wavelength of the laser beam is large compared to the size of an atom, we can neglect $\mathbf{k} \cdot \mathbf{r} = 2\pi r/\lambda \ll 1$ for r less than or equal

the atom size. This approximation, when connected with a dipole-field interaction (see Eq. (2.61)), is called the *dipole approximation*. We can also drop the phase shift ϕ, since it will make no difference to the final result, which consists in determining the probabilities of electrons occupying the two possible levels. We shall use only the real part of $\mathbf{E}$ from Eq. (1.8):

$$\mathbf{E} = \mathbf{E}_0 \cos \omega t = \frac{\mathbf{E}_0}{2}(e^{i\omega t} + e^{-i\omega t}). \tag{2.60}$$

Hence, our Hamiltonian

$$H = H_0 + \boldsymbol{\mu} \cdot \mathbf{E} \tag{2.61}$$

in the dipole approximation reads

$$H = H_0 - e\mathbf{r} \cdot \mathbf{E}_0 \cos \omega t. \tag{2.62}$$

It determines the Schrödinger equation

$$H\Psi = i\hbar \frac{\partial \Psi}{\partial t} \tag{2.63}$$

whose general solution for our two-level system is

$$|\Psi\rangle = c_g(t)e^{-iE_g t/\hbar}|g\rangle + c_e(t)e^{-iE_e t/\hbar}|e\rangle, \tag{2.64}$$

where $|g\rangle$ and $|e\rangle$ are the base states (ground and excited). Taking into account that

$$H_0|g\rangle = E_g|g\rangle \qquad \text{and} \qquad H_0|e\rangle = E_e|e\rangle \tag{2.65}$$

by introducing Eq. (2.64) into Eq. (2.63) and carrying out the spatial integration, we get [Demtröder, 1996, 2.6.2]

$$\frac{dc_g(t)}{dt} = \frac{iR_{eg}}{2}\left[e^{-i(\omega_{eg}+\omega_L)t} + e^{-i(\omega_{eg}-\omega_L)t}\right] c_e(t), \tag{2.66}$$

$$\frac{dc_e(t)}{dt} = \frac{iR_{eg}}{2}\left[e^{i(\omega_{eg}+\omega_L)t} + e^{i(\omega_{eg}-\omega_L)t}\right] c_g(t), \tag{2.67}$$

where $\omega_{eg} = (E_e - E_g)/\hbar$ and $R_{eg} = D_{eg}E_0/\hbar = R_{eg}$, where D_{eg}, a spatial integral of $\langle g|\mathbf{p} \cdot \mathbf{E}|e\rangle$, is called the *atomic dipole matrix element*—it is determined by the charge distribution in the states $|g\rangle$ and $|e\rangle$. We see that, on the right side of Eq. (2.66), we have only $c_e(t)$, and in Eq. (2.67) only $c_g(t)$. This is because $D_{gg} = D_{gg} = 0$. Physically, it means that $|e\rangle$ can only evolve from $|g\rangle$, and $|g\rangle$ only from $|e\rangle$.

For $\omega_L \approx \omega_{eg}$, the terms containing $\exp[\mp i(\omega_{eg} + \omega_L)t]$ in Eqs. (2.67) and (2.66) oscillate rapidly in time and can be neglected with respect to the near resonant terms, i.e., the terms containing $\exp[\mp i(\omega_{eg} - \omega_L)t]$. This approximation is called the *rotating wave approximation*, in which Eqs. (2.67) read [Demtröder, 1996, 2.6.6]

$$\begin{aligned} \frac{dc_g(t)}{dt} &= \frac{iR_{eg}}{2} e^{-i(\omega_{eg}-\omega_L)t} c_e(t), \\ \frac{dc_e(t)}{dt} &= \frac{iR_{eg}}{2} e^{i(\omega_{eg}-\omega_L)t} c_g(t). \end{aligned} \tag{2.68}$$

Their solutions are

$$\begin{aligned} c_g(t) &= \frac{1}{\mu_1 - \mu_2} \left(\mu_1 e^{i\mu_2 t} - \mu_2 e^{i\mu_1 t}\right), \\ c_e(t) &= \frac{iR_{eg}}{\Omega} e^{i(\omega_{eg}-\omega_L)t/2} \sin\frac{\Omega t}{2}, \end{aligned} \tag{2.69}$$

where

$$\begin{aligned} \mu_{1,2} &= -\frac{1}{2}(\omega_{eg} - \omega_L) \pm \sqrt{(\omega_{eg} - \omega_L)^2 + R_{eg}^2}, \\ \Omega &= \mu_1 - \mu_2 = \sqrt{(\omega_{eg} - \omega_L)^2 + R_{eg}^2}. \end{aligned} \tag{2.70}$$

Eqs. (2.69) gives the transition probabilities

$$|c_e(t)|^2 = \left(\frac{R_{eg}}{\Omega}\right)^2 \sin^2\frac{\Omega t}{2}, \qquad |c_g(t)|^2 = 1 - |c_e(t)|^2, \tag{2.71}$$

which oscillate with frequency Ω—called the *Rabi flopping frequency*—between levels E_g and E_e.

For instance, at resonance ($\omega_L = \omega_{eg}$) after a time $T = \pi/\Omega = \pi/R_{eg}$ the probability of finding the system in level E_e is 1. This result means we will have the following evolution:

$$\begin{aligned} |c_g(0)|^2 = 1 \;&\rightarrow\; |c_g(T)|^2 = 0, \qquad \text{and} \\ |c_e(0)|^2 = 0 \;&\rightarrow\; |c_e(T)|^2 = 1, \end{aligned} \tag{2.72}$$

i.e., full control over the states of the electron in time.

We note here that, in the literature, R_{eg} is often called the *Rabi frequency* and denoted Ω_{eg} whenever $\omega_L = \omega_{eg}$ or when only $\omega_L \approx \omega_{eg}$ because Eq. (2.70) then reads $\Omega = R_{eg}$ and $\Omega \approx R_{eg}$, respectively. For

example, Eq. (2.68) would in this notation read[4]

$$\begin{bmatrix} \frac{dc_g}{dt} \\ \frac{dc_e}{dt} \end{bmatrix} = \frac{i\Omega_{eg}(t)}{2} \begin{bmatrix} 0 & e^{-(i\omega_{eg}-\omega_L)t} \\ e^{i(\omega_{eg}-\omega_L)t} & 0 \end{bmatrix} \begin{bmatrix} c_g \\ c_e \end{bmatrix}. \tag{2.73}$$

So far, we have used a semiclassical description of the interaction between a two-level atom and a laser field. A quantum description of the interaction would require a quantization of the radiation field and dealing with its Fock states, i.e., photon number states. This description is known as the *Jaynes–Cummings model.* However, since the model essentially serves as a bridge to a model describing the interaction of a laser field and collective modes of trapped ions—a formal similarity between photon and phonon behavior has been recognized [Cirac et al., 1993]—we can dwell directly on the laser beam–electron–phonon interaction as presented in [Cirac and Zoller, 1995].

To this end, we shall repeat the above procedure, starting again with the electric field given by Eq. (2.59) and the Hamiltonian (2.61). However, we shall not use the dipole approximation (Eqs. (2.61) and (2.62)), because a laser beam that acts on ions should not only induce transitions between their ground and excited levels but also change the states of their collective modes. Since the direction and amount of the wave vector $\mathbf{k}$ of a laser beam must be taken into account to describe its interaction, the term $\mathbf{k} \cdot \mathbf{r}$ cannot be neglected as in the dipole approximation. Instead, we start with [Sørensen and Mølmer, 1999; Sørensen and Mølmer, 2000]

$$H = H_0 + H_{\text{int}} = H_{\text{col}} + H_{\text{el}} + H_{\text{int}}, \tag{2.74}$$

where H_{col} is the Hamiltonian of the collective ion mode given by Eq. (2.56); the laser beam–ion interaction term H_{int} is

$$H_{\text{int}} = \boldsymbol{\mu} \cdot \mathbf{E} \tag{2.75}$$

where $\boldsymbol{\mu}$ is an electric dipole created in the ion; and H_{el} can be expressed as

$$H_{\text{el}} = \sum_j E_j \varepsilon_j^\dagger \varepsilon_j, \tag{2.76}$$

[4]We are going to refer to Eqs. (2.68) and (2.73) in Sec. (3.1.4) (p. 142) while deriving an equivalent equation—Eq. (3.4)—for three levels, and the references we are going to cite in Sec. (3.1.4) will make use of the Rabi frequency notation.

where $\varepsilon^\dagger$ and ε are electron creation and annihilation operators, respectively. Note that electrons are fermions and that ε and $\varepsilon^\dagger$ satisfy the following commutation relations (cf. Eq. (2.57)):

$$\varepsilon_j^\dagger \varepsilon_k - \varepsilon_k \varepsilon_j^\dagger = \delta_{jk}. \tag{2.77}$$

To describe the Jaynes–Cummings model, one usually makes use of a formal analogy between a two-level atom and a spin $\frac{1}{2}$ system in a magnetic field. Such an analogy has been used for descriptions of trapped-ion models as well [Cirac et al., 1993]. It consists in calling the electric dipole $\boldsymbol{\mu}$ and the electric field $\mathbf{E}$ from Eq. (2.61) a *fictitious magnetic dipole* $\boldsymbol{\mu}_\sigma$ and a *fictitious magnetic field* $\mathbf{B}_\sigma$, respectively. This enables us to introduce *fictitious spin operators* σ^+, σ^-, and σ_z as follows.

The main aim of such fictitious operators is to simplify the state notation. In the number state notation, we denote the vacuum state by $|0\rangle$ and a state occupied by one electron by $|1\rangle$. So the ground state in a two-level system is denoted by $|10\rangle = |1,0\rangle = |1\rangle|0\rangle$ and the excited state by $|01\rangle = |0,1\rangle = |0\rangle|1\rangle$. However, since in quantum optics we are mainly concerned with single electrons, it is practical to reduce this two-state formalism to a one-state formalism. To do this, let us look at the actions of the *Fermi operators*:

$$\varepsilon_1^\dagger \varepsilon_2 |01\rangle = \varepsilon_1^\dagger |00\rangle = |10\rangle \qquad \varepsilon_1^\dagger \varepsilon_2 |10\rangle = 0. \tag{2.78}$$

We shall deal neither with $|00\rangle$ nor with $|11\rangle$, but if we did, we would get $\varepsilon_1^\dagger \varepsilon_2 |00\rangle = 0$ and $\varepsilon_1^\dagger \varepsilon_2 |11\rangle = 0$, respectively. (We have $\varepsilon^\dagger |1\rangle = 0$ because electrons are fermions, and two of them cannot occupy the same state.) Similarly, we have

$$\varepsilon_2^\dagger \varepsilon_1 |01\rangle = 0, \qquad \varepsilon_2^\dagger \varepsilon_1 |10\rangle = \varepsilon_2^\dagger |00\rangle = |01\rangle, \tag{2.79}$$

$$(\varepsilon_2^\dagger \varepsilon_2 - \varepsilon_1^\dagger \varepsilon_1)|01\rangle = |01\rangle, \qquad (\varepsilon_2^\dagger \varepsilon_2 - \varepsilon_1^\dagger \varepsilon_1)|10\rangle = -|10\rangle. \tag{2.80}$$

If we now introduce (bearing in mind that we shall deal neither with $|00\rangle$ nor with $|11\rangle$)

$$|01\rangle = |g\rangle = \begin{bmatrix} 0 \\ 1 \end{bmatrix} \qquad \text{and} \qquad |10\rangle = |e\rangle = \begin{bmatrix} 1 \\ 0 \end{bmatrix} \tag{2.81}$$

in analogy with Eqs. (2.78) and (2.79), we have

$$\sigma^+ |g\rangle = \sigma^+ \begin{bmatrix} 0 \\ 1 \end{bmatrix} = \begin{bmatrix} 1 \\ 0 \end{bmatrix} = |e\rangle, \qquad \sigma^+ |e\rangle = 0,$$

$$\sigma^- |g\rangle = 0, \qquad \sigma^- |e\rangle = \sigma^- \begin{bmatrix} 1 \\ 0 \end{bmatrix} = \begin{bmatrix} 0 \\ 1 \end{bmatrix} = |g\rangle, \tag{2.82}$$

where

$$\sigma^+ = \frac{1}{2}(\sigma_x + i\sigma_y) = \begin{bmatrix} 0 & 1 \\ 0 & 0 \end{bmatrix}, \quad \sigma^- = \frac{1}{2}(\sigma_x - i\sigma_y) = \begin{bmatrix} 0 & 0 \\ 1 & 0 \end{bmatrix}, \tag{2.83}$$

where σ_x and σ_y are the Pauli matrices defined in Eq. (1.88). Also, in analogy with Eq. (2.80), we have

$$\sigma_z|g\rangle = |g\rangle \qquad \text{and} \qquad \sigma_z|e\rangle = -|e\rangle, \tag{2.84}$$

where the Pauli matrix σ_z is given by Eq. (1.88).

Thus the Hamiltonian H_{el} given by Eq. (2.76),

$$H_{\text{el}} = E_e\varepsilon_2^\dagger\varepsilon_2 + E_g\varepsilon_1^\dagger\varepsilon_1, \tag{2.85}$$

can be written as

$$\begin{aligned} H_{\text{el}} &= \frac{1}{2}E_{eg}(\varepsilon_2^\dagger\varepsilon_2 - \varepsilon_1^\dagger\varepsilon_1) + \frac{1}{2}(E_e + E_g)(\varepsilon_2^\dagger\varepsilon_2 + \varepsilon_1^\dagger\varepsilon_1) \\ &= \frac{1}{2}E_{eg}\sigma_z + \frac{1}{2}(E_e + E_g)\mathbb{1} = \frac{1}{2}\omega_{eg}\hbar\sigma_z + \frac{1}{2}(E_e + E_g)\mathbb{1}, \end{aligned} \tag{2.86}$$

where $E_{eg} = E_e - E_g$. By redefining the zero-energy so as to put it in between E_e and E_g, as shown in Fig. 2.16 (p. 113, we get

$$H_{\text{el}} = \frac{1}{2}\omega_{eg}\hbar\sigma_z, \qquad H_{\text{el}}|g\rangle = -\frac{1}{2}\omega_{eg}|g\rangle, \qquad H_{\text{el}}|e\rangle = \frac{1}{2}\omega_{eg}|e\rangle. \tag{2.87}$$

In a similar way, we can redefine H_{col} from Eq. (2.74) given by Eq. (2.56) so as to suppress the zero-point energy $\hbar\omega_z/2$. Hence we obtain

$$H_0 = H_{\text{col}} + H_{\text{el}} = \hbar\omega_z a^\dagger a + \frac{1}{2}\omega_{eg}\hbar\sigma_z. \tag{2.88}$$

The interaction term H_{int} (2.75) of our Hamiltonian (2.74) is [Wineland et al., 1998; Wineland et al., 2003]

$$H_{\text{int}} = \boldsymbol{\mu}\cdot\mathbf{E} = \mu(\sigma^+ + \sigma^-)E_0\cos(\mathbf{k}\cdot\mathbf{r} - \omega_L t + \phi). \tag{2.89}$$

To simplify the presentation and the equations, we have assumed (without loss of generality) that $\mathbf{r}$ (the ion position operator with respect to the equilibrium position of the ion) is oriented along the axis of the trap and that the wave vector $\mathbf{k}$, i.e., the laser beam, is also oriented along that axis. So we have

$$r = z = z_0(a + a^\dagger), \qquad \text{where} \qquad z_0 = \sqrt{\langle 0|z|0\rangle} = \sqrt{\frac{\hbar}{2m\omega_z}}. \tag{2.90}$$

The electric field is assumed to be polarized along the x-axis, and thus the electric dipole $\boldsymbol{\mu}$ is an operator for the internal transition. Therefore, it is, in analogy with electronic spin (see Eq. (2.6)), proportional to $\sigma_x = \sigma^+ + \sigma^-$; ϕ is the phase of the laser beam at the equilibrium position of the ion, and E_0 is the amplitude of the laser wave.

Taken together, we have

$$H_{\text{int}} = \hbar\Omega(\sigma^+ + \sigma^-)\left\{e^{i[\eta(a+a^\dagger)-\omega_L t+\phi]} + e^{-i[\eta(a+a^\dagger)-\omega_L t+\phi]}\right\}, \quad (2.91)$$

where $\eta = kz_0$ is called the *Lamb–Dicke parameter* and Ω is the Rabi frequency (cf. Eq. (2.71)) and is in our case $\Omega = \mu E_0/(4\hbar)$. (Recall that $\sigma^+ = |e\rangle\langle g|$ and $\sigma^- = |g\rangle\langle e|$.)

Now the laser beam we use for manipulating the ions we also use for cooling the ions further, after the Doppler cooling reaches its limits. A tuned laser beam allows an ion to run up a dipole potential hill (thus losing energy); then, before the ion can run down again and regain the energy, it pumps the ion into another ground state with a lower potential hill. Then the ion returns to the former ground state via another laser pumping, and the whole process starts again. With each cycle, the ion loses some energy, and since it always goes up the potential hill more often than down, the cooling is called *Sisyphus cooling* [Wineland et al., 1992]. To make such cooling possible, the characteristic length scale of motion of the ion must be much smaller than the wavelength of the exciting laser beam. This is called the *Lamb–Dicke limit.* It implies that the frequency of the ion modes (ω_z, $\sqrt{3}\omega_z$, ...) must be larger than the recoil frequency corresponding to the transition used for laser cooling. Actually, the exploration of such cooling processes brought the researchers to the idea of using the same mechanisms for quantum computing, and the teams that were previously engaged in the cooling of atoms were the first to propose and implement ion computing [Wineland and Itano, 1979; Blatt et al., 1986; Wineland et al., 1992; Cirac et al., 1992].

For our purpose of understanding how qubits can be implemented in ion traps, an elaboration of the Hamiltonian (2.91) turns out to be important—namely, its presentation in the interaction picture (in which both the state functions and operators are time dependent) [Greiner, 1989, 10.9]. Starting with the Scrödinger equation

$$(H_0 + H_{\text{int}})\Psi = i\hbar\frac{d\Psi}{dt}, \quad (2.92)$$

we make the transformation

$$\Psi = U\Psi', \qquad \text{where} \qquad U = e^{-iH_0 t/\hbar}, \quad (2.93)$$

and obtain

$$H'_{\text{int}}\Psi' = i\hbar\frac{d\Psi'}{dt}, \qquad \text{where} \qquad H'_{\text{int}} = U^{\dagger}H_{\text{int}}U. \tag{2.94}$$

To transform the Hamiltonian (2.91) into the interaction picture, we use the following relations between the Schrödinger and interaction picture operator forms:

$$\varepsilon'_1 = \varepsilon_1 e^{-i\omega_g t}, \qquad \varepsilon'_2 = \varepsilon_2 e^{-i\omega_e t}, \qquad \text{and} \qquad a' = ae^{-i\omega_z t}. \tag{2.95}$$

Since σ^+ corresponds to $\varepsilon_2^{\dagger}\varepsilon_1$ and since $\sigma^- = (\sigma^+)^{\dagger}$ [see Eq. (2.83)], we get

$$\sigma'^{+} = \sigma^+ e^{i\omega_{eg}t}, \qquad \sigma'^{-} = \sigma^- e^{-i\omega_{eg}t}, \qquad \text{and} \qquad a'^{\dagger} = a^{\dagger}e^{i\omega_z t}. \tag{2.96}$$

By introducing these operators into Eq. (2.91), we get an expression with the terms containing

$$e^{-i(\omega_{eg}+\omega_L)t} \qquad \text{and} \qquad e^{-i(\omega_{eg}-\omega_L)t}, \tag{2.97}$$

as well as the terms containing their conjugates.

Here, as in Eq. (2.67), we can apply the *rotating wave approximation* for $\omega_L \approx \omega_{eg}$ and neglect the terms containing $\exp[\mp i(\omega_{eg} + \omega_L)t]$, which rapidly oscillates in time with respect to the terms containing near resonant $\exp[\mp i(\omega_{eg} - \omega_L)t]$. Thus Eq. (2.91) yields our Hamiltonian in the interaction picture:

$$H'_{\text{int}} = \hbar\Omega\sigma^+ e^{i[\eta(ae^{-i\omega_z t}+a^{\dagger}e^{i\omega_z t})-\delta+\phi]} + \text{H.c.}, \tag{2.98}$$

where $\delta = \omega_L - \omega_{eg}$ and H.c. means the *Hermitian conjugate.* The corresponding wave function for the first two collective modes is

$$\Psi' = C_{g,0}(t)|g\rangle|0\rangle + C_{g,1}(t)|g\rangle|1\rangle + C_{e,0}(t)|e\rangle|0\rangle + C_{e,1}(t)|e\rangle|1\rangle. \tag{2.99}$$

Of primary interest for quantum computing will be the resonant transitions $\delta = (n' - n)\omega_z$, where $n, n' = 0, 1$.

By introducing Ψ' from Eq. (2.99) into Eq. (2.94), we get, in fashion similar to Eq. (2.67) [Wineland et al., 1998],

$$\begin{aligned}\frac{dC_{e,n'}}{dt} &= -i^{1+|n'-n|}e^{i\phi}\Omega_{n',n}C_{g,n},\\ \frac{dC_{g,n'}}{dt} &= -i^{1-|n'-n|}e^{-i\phi}\Omega_{n',n}C_{e,n'},\end{aligned} \tag{2.100}$$

where

$$\Omega_{n',n} = \Omega|\langle n'|e^{i\eta(a+a^{\dagger})}|n\rangle| = \Omega e^{-\eta^2/2}\sqrt{\frac{n_<!}{n_>!}}\eta^{|n'-n|}L_{n_<}^{|n'-n|}(\eta^2), \tag{2.101}$$

where $n_>$ ($n_<$) is the greater (smaller) of n' and n, and L_n^α is the generalized Laguerre polynomial

$$L_n^\alpha(X) = \sum_{m=0}^{n} (-1)^m \binom{n+\alpha}{n-m} \frac{X^m}{m!} . \tag{2.102}$$

In ion quantum computing experiments, we are primarily interested in $n' = n, n \mp 1$ (in particular, in $n = 0, 1$). The corresponding $\omega_L = \omega_{eg}$, $\omega_{eg} \mp \omega_z$ are called the *carrier, red sideband*, and *blue sideband* frequencies, respectively.

Upon solving Eq. (2.100), we get [Wineland et al., 1998]

$$\begin{aligned} |n\rangle|g\rangle &\to \cos\Omega_{n',n}t|n\rangle|g\rangle - ie^{i(\phi+\frac{\pi}{2}|n'-n|)} \sin\Omega_{n',n}t|n'\rangle|e\rangle, \\ |n\rangle|e\rangle &\to -ie^{i(\phi+\frac{\pi}{2}|n'-n|)} \sin\Omega_{n',n}t|n\rangle|g\rangle + \cos\Omega_{n',n}t|n'\rangle|e\rangle. \end{aligned} \tag{2.103}$$

For the carrier frequency ($n' = n$), we can write Eq. (2.103) as

$$\begin{aligned} |n\rangle|g\rangle &\to \cos\Omega_{n,n}t|n\rangle|g\rangle - ie^{i\phi} \sin\Omega_{n,n}t|n\rangle|e\rangle \\ |n\rangle|e\rangle &\to -ie^{i\phi} \sin\Omega_{n,n}t|n\rangle|g\rangle + \cos\Omega_{n,n}t|n\rangle|e\rangle, \end{aligned} \tag{2.104}$$

where $\Omega_{n,n}$, for $n = 0, 1$, we are going to use, follow from Eq. (2.101):

$$\Omega_{0,0} = \Omega e^{-\eta^2/2}, \qquad \Omega_{1,1} = \Omega e^{-\eta^2/2}(1-\eta^2). \tag{2.105}$$

Therefore, with a proper choice of laser pulse duration and phase, we can use $|g\rangle$ and $|e\rangle$ as single qubit states to set up a single qubit gate (see Sec. 1.18, p. 45). For example, for a laser pulse of duration $t = \pi/\Omega_{n,n}$ and a phase $\phi = -\pi/2$, we get the NOT gate (1.32). On the other hand, $t = \pi/(2\Omega_{n,n})$, $\phi = -\pi/2$, and a rotation about the z-axis give a Hadamard gate (1.59).

To construct a CNOT gate, we need a two-qubit system, and for that purpose we can use a single ion with collective states $|0\rangle$ and $|1\rangle$ as the control qubit states and $|g\rangle$ and $|e\rangle$ as the target qubit states. Thus we will have

$$|00\rangle = |0\rangle|g\rangle, \quad |01\rangle = |0\rangle|e\rangle, \quad |10\rangle = |1\rangle|g\rangle, \quad |11\rangle = |1\rangle|e\rangle. \tag{2.106}$$

Our aim is to swap $|g\rangle$ and $|e\rangle$ whenever the ion is in state $|1\rangle$ and to leave them unchanged whenever it is in $|0\rangle$—by a single laser pulse. To achieve this aim, Monroe, Leibfried, King, Meekhof, Itano, and Wineland [Monroe et al., 1997] set the Lamb–Dicke parameter η so that[5]

$$\frac{\Omega_{1,1}}{\Omega_{0,0}} = \frac{2k+1}{2m}. \tag{2.107}$$

[5]Alternative CNOT implementations have been put forward by Cirac and Zoller [Cirac and Zoller, 1995; Poyatos et al., 2000].

This can be done by choosing (see Eq. (2.105))

$$\eta = \sqrt{1 - \frac{2k+1}{2m}}. \tag{2.108}$$

Now, driving the laser carrier transition for a duration of $t = (k + 1/2)/\Omega_{1,1}$ is equivalent to driving it for $t = (2m)/\Omega_{0,0}$. Hence, Eq. (2.104) for $k = 0$, $m = 1$, ($\eta = 0.707$), and $\phi = -\pi/2$ yields

$$\begin{aligned}
|00\rangle &\rightarrow \cos 2\pi|0\rangle|g\rangle - ie^{-i\pi/2}\sin 2\pi|0\rangle|e\rangle = |00\rangle \\
|01\rangle &\rightarrow -ie^{-i\pi/2}\sin 2\pi|0\rangle|g\rangle + \cos 2\pi|0\rangle|e\rangle = |01\rangle, \\
|10\rangle &\rightarrow \cos\frac{\pi}{2}|1\rangle|g\rangle - ie^{-i\pi/2}\sin\frac{\pi}{2}|1\rangle|e\rangle = |11\rangle \\
|11\rangle &\rightarrow -ie^{i\phi}\sin\frac{\pi}{2}|1\rangle|g\rangle + \cos\frac{\pi}{2}t|1\rangle|e\rangle = |10\rangle,
\end{aligned} \tag{2.109}$$

which is nothing but a CNOT gate.

To read out the result of a completed calculation the states of all qubits must be measured. For example, let the $|0\rangle$ state of a qubit be a ground state of an ion and $|1\rangle$ a metastable excited state of the ion, as in Fig. 3.3 (p. 140). We can interrogate the qubit with a laser beam tuned to excite the electron from the ground state to an excited state (the transition at 397 nm in Fig. 3.3, p. 140). If the ion then emits a photon, this means that the ion was in the ground state. If it does not emit a photon, it is in the metastable level (the laser beam does not "see" the ion; it can be seen there only by a laser tuned to a transition from the metastable to the excited level—866 nm).

In Sec. 1.22 (p. 72), we have seen that by using single qubit and CNOT gate we can entangle qubits. However, we have also seen (in Sec. 1.20, p. 56) that entangling photons requires selecting appropriate states and throwing away the remaining events. An ion computer can do the entanglement better. It can *deterministically* entangle states *on demand* without throwing away any events [Kielpinski et al., 2002]. An immediate consequence is deterministic quantum teleportation of qubits around ion computer circuits and nets [Barrett et al., 2004].

Since any quantum circuit can be constructed by means of single qubit gates and CNOT gates, the ion computer proves to be universal, and since any two ion states can be entangled no matter how far away from each other they are in the trap, the ion computer is scalable in principle. There are several proposals on how to scale up to realistic ion computers. One way is to store ions in an array of microtraps, which can be realized by electric and/or laser fields as shown in Fig. 2.17 [Cirac and Zoller, 2000]. The key idea is to address neighboring ions conditionally, based on their state, as opposed to the exchange of phonons corresponding to

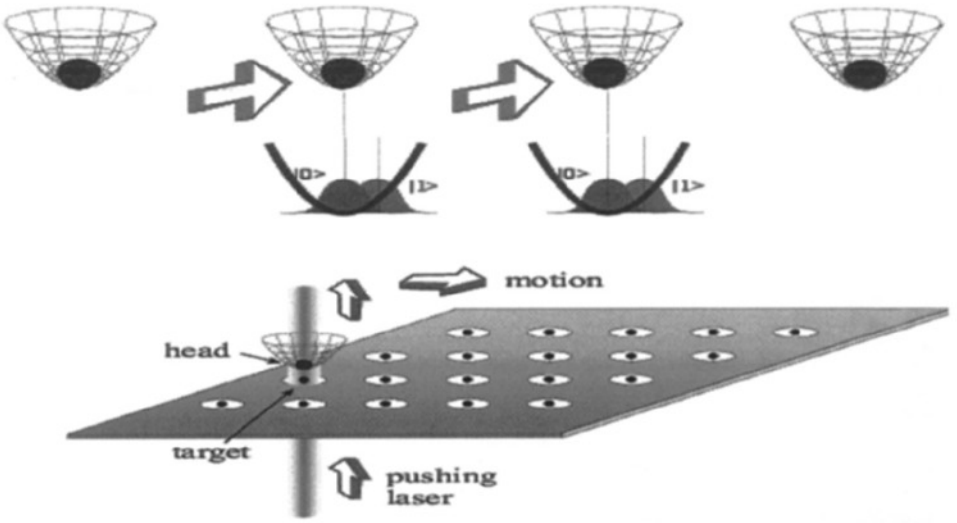

Figure 2.17. A scale-up proposal for ion computers by means of arrays of microtraps, which can be realized by electric and/or laser fields [Cirac and Zoller, 2000].

the collective center-of-mass motion of the ions in the model presented above. Another model is a *quantum charge-coupled device* architecture consisting of a large number of interconnected ion traps in each of which one can manipulate a few ions using the methods demonstrated above [Kielpinski et al., 2002]. All in all, these models are technological challenges for future development.

2.6 Future Experiments

There are five generally accepted requirements for the implementation of quantum computation:

1. A scalable physical system with well-characterized qubits,
2. The ability to initialize the state of the qubits to a simple reliable state ($|000...\rangle$),
3. Long decoherence times, much longer than the gate operation time,
4. A universal set of quantum gates,
5. A qubit-specific measurement capability,

and two additional networkability conditions:

6. The ability to interconvert stationary and flying qubits,
7. The ability to faithfully transmit flying qubits between specified locations.

These requirements are called the *DiVincenzo Criteria* [DiVincenzo, 2000].

We have seen that the trapped-ion computer satisfies all these criteria, while the Kane solid state computer satisfies the first five—for the sixth and seventh, it is too early to decide. A number candidates that satisfy most of these criteria, and there are many more candidates that only partially (at least for the time being) satisfy them (see Table 2.1). Consequently, we cannot have a "winner" at the present stage of research. The challenges facing the realization of this project are tremendous, but still it is expected that the current experimental advances will lead us to a winner eventually. A better understanding of the quantum behavior of quantum systems is needed before promising candidates can be engineered to a larger scale. To help scientists and students on the road to a realistic quantum computer and to enable an informed comparison of different projects, a panel of experts in experimental implementations of quantum computing systems has compiled a report under the name *A Quantum Information Science and Technology Roadmap: Part 1. Quantum Computation* [Hughes et al., 2004]. In the report, all presently pursued quantum computing systems have been compared, results reviewed, and references given.

Table 2.1. Promising criteria for quantum computation candidates according to [Hughes et al., 2004]. "+" means *a potentially viable approach with sufficient proof of principle*, "±" means *a potentially viable approach without sufficient proof of principle*, and "−" means *no viable approach is known.*

	DiVincenzo Criteria						
Candidates	1	2	3	4	5	6	7
NMR	−	±	±	+	±	−	−
Solid State	±	±	±	±	±	−	−
Trapped Ion	±	+	±	+	+	±	±
Cavity QED	±	+	±	±	+	±	±
Neutral Atom	±	+	±	±	±	±	±
Optical	±	±	+	±	±	±	+
Superconducting	±	+	±	±	±	−	−
"Unique" Qubits	a variety of criteria evaluation						

Altogether there are over hundred different systems and subsystems used for implementing qubits by almost as many teams all over the world. Consequently, we are currently gaining an abundance of new results on the engineering of quantum systems together with more and more functional quantum computation systems. At the present level of the experimental effort all over the world, a quantum computer with up to 50 qubits and with error-correcting code will most likely appear by

2012. Whether we will be able to construct a quantum computer that will surpass the fastest classical computers in the near future remains to be seen. It is estimated that such a computer should have more than 1000 qubits and should be able to carry out more than 10^9 operations [Preskill, 1998], and this project will probably be attempted for only one or two "winners." The history of classical computing indicates that we might have its quantum "super-counterpart" sooner than later.

2.7 Quantum Communication Implementation

In contrast to quantum computation experiments, quantum communication experiments are at the moment split into those that are almost ahead of their theory—quantum cryptography—and those that have barely started and for which the first extensive implementations are expected after 2012—qubit DiVincenzo networkability (see DiVincenzo criteria 6 and 7 in Sec. 2.6, p. 124). Therefore, in this section, we will limit ourselves to a brief quantum cryptography implementation overview.

Quantum cryptography is entering its physical and industrial application stage. The protocols currently being used in applications are essentially those proposed two decades ago (see Secs. 1.23 and 1.23), although there are also new proposals. At least three companies, BBN Technologies (Cambridge, MA, USA), ID Quantique (Geneva, Switzerland) and MagiQ Technologies (New York, NY, USA), have released commercial quantum cryptography (quantum key distribution, QKD) systems, and several others are about to do so. These products are still not cost-effective for commercial applications. They can be regarded as prototypes supported by multimillion dollar government-, publicly, and privately funded projects [Ouellette, 2005].[6]

As the most important project, we single out the World's first quantum network—the DARPA quantum network—fully operational since October 23, 2003 [Elliott et al., 2005]. This is a joint project of BBN Technologies, Harvard University, and Boston university, technologically

[6]The following funding allocations include quantum cryptography: DARPA of the Department of Defense (DoD) (2002–2007) with $50 million (Quantum Information Science and Technology, QuIST program); in Europe, Quantum Information Processing and Communications (5th and 6th EU Framework Programme) (1998–2007), about $80 million; in Japan, Japanese Government Organisations Sponsoring Nanotechnology R&D $2.75 billion/year. Similar funding exist in Australia, Australasia, and Canada, including many private contributions; for example, in 2004 a single private donation (by Ophelia and Mike Lazaridis) for quantum computing research in Canada to a single institution (University of Waterloo) reached $33 million].

implemented by BBN Technologies, and supported by DARPA.[7] The DARPA quantum network spans 29 km and does take an eavesdropper (Eve) into account. Two kinds of error correction schemes are implemented in the network and therefore, at least in principle, the network can be considered unconditionally secure.

Since higher rigorous distance limits are essential for successful implementations of QKD systems, researchers are now mostly focused on physical solutions that can increase this limit. Most applications and experiments use optical fibers to connect Alice to Bob or a common EPR source to Alice and Bob. Free space transmission suffers high losses (the present distance limit is about 25 km), but a possible ground–satellite–ground communication is also a research goal. There are three main problems here: the medium, the source, and the detector. The lowest losses in fibers occur near the 1550 nm wavelength—with about 50% loss after about 15 km—which is why these wavelengths are widely used by the telecommunications industry. Unfortunately, the best commercially available single-photon counters operate near 800nm. Thus, better 1550 nm would be desirable. The photon source is a particularly difficult problem. and we consider it next. The potential and status of various proposed implementations were presented in the report *Quantum Information Science and Technology Roadmap: Part 1. Quantum Cryptography* [Bennett et al., 2004], compiled by a panel of quantum cryptography technology experts and shown in Table 2.2.

Table 2.2. Attributes of quantum cryptography implementations: 1. Theoretical security status; 2. Distance limit potential; 3. Speed (bit/sec) potential; 4. Maturity (application readiness); 5. Robustness. Scores given: '+' *high*, '±' *medium*, '−' *low*. According to [Bennett et al., 2004].

	Attributes				
Implementations	1	2	3	4	5
Weak laser pulses	±	+	+	±	±
Single-photon source	+	+	±	−	±
Entangled pairs	+	+	±	±	±
Continuous variables	−	−	+	−	−

Most implementations of quantum cryptography rely on weak laser pulses generated by conventional *diode lasers* over optical fibers because this approach enables the use of present telecommunications technology. We attenuate the laser pulse so that it contains less than one photon in

[7] DARPA is the Defense Advanced Research Projects Agency, the central research and development organization for the Department of Defense (DoD) of USA.

a time window. Most experiments so far used a mean photon number $\mu = 0.1$. The probability of detecting n photons in a pulse, under the assumption that the detections are statistically independent, is given by the *Poisson distribution*, which applies when we approximate the single-photon Fock state by a coherent photon state with a very low μ [Gisin et al., 2002]

$$P(n, \mu) = \frac{\mu^n}{n!} e^{-\mu}. \tag{2.110}$$

Therefore, the conditional probability that a nonempty coherent laser pulse contains more than one photon is given by

$$P(n > 1 | n > 0, \mu) = \frac{1 - P(0, \mu) - P(1, \mu)}{1 - P(0, \mu)} \approx \frac{\mu}{2}. \tag{2.111}$$

Hence, $\mu = 0.1$ means that 5% of nonempty pulses contain more than one photon. Two or more photons per pulse jeopardizes the security of the key transmission the most, since Eve can always split the pulse and let one photon through without changing its state. This approach allows her to learn about the corresponding bit without being caught. We cannot go much below $\mu = 0.1$ with the standard approach, because of the *dark counts* (the detector clicks without photons actually arriving at the detector), This is also an issue with today's detectors. We can hope for a development in detector technology that will decrease detector noise. However, recently a novel approach has been put forward that enables us, in effect, to go five times below $\mu = 0.1$ with existing technology [Hwang, 2003].

The approach consists in catching an eavesdropper (Eve) by means of decoy (fake) pulses that a sender (Alice) sends to a receiver (Bob) in addition to proper signal pulses. The signal and decoy pulses differ only in their photon number distributions (intensities). For instance, suppose $\mu_{\text{decoy}-1} = 0$, $\mu_{\text{decoy}-2} = 0.02$, and $\mu_{\text{signal}} = 0.1$. Eve cannot distinguish a decoy state from a signal state when she splits the pulse. Bob, however, can tell whether Eve has split a decoy pulse or not—the error rates will differ—and if he finds she has, he will abort the transmission. It can be shown that the key generator rate achieves a substantial increase and that the secure QKD is possible over much longer distances than with the standard approach.

Single-photon sources get around the problem of the photon number splitting attack problem since the sources are not probabilistic but deterministic. Ideally, and in principle, they produce n photons "on demand" rather than on average. Such a source is also called a *photon gun*. The first promising experiments on this approach were done in 1998–2000.

They were mostly concentrated on single two-level individual atoms, which would be excited by means of a laser beam of one frequency and subsequently would emit a fluorescence photon at another [Gisin et al., 2002]. The moment of emission can be controlled as shown in Sec. 2.5 [Eqs. (2.70) and (2.71)]. The main problem was the collection efficiency (under 0.1%), since photons from free atoms are in general not emitted in a predetermined direction.

A second approach uses photon emission of electron-hole pairs in a semiconductor quantum dot. An electron-hole pair created in the dot by optical pumping recombines and emits photons at different frequencies, each of which can be distinguished by a filter [Gisin et al., 2002]. Another proposal uses single quantum dots and Weierstrass solid immersion lenses that facilitate light collection [Zwiller et al., 2004].

The third approach is the most demanding but apparently also the most promising. It consists in obtaining fluorescence photons by manipulating trapped atoms or ions and is closely connected to quantum computation with trapped ion systems and cavity QED systems (see Sec 2.5, p. 109). For the most recent papers on all three approaches the reader is directed to the recent *Focus on Single Photons on Demand* [Grangier et al., 2004].

The *entangled pair approach* from Table 2.2[8] aims at increasing the distance limit as well as the security against eavesdropping. In an optical fiber, the probability of absorption of a photon as well as of its depolarization increases exponentially with the length of the fiber. The Malus law (1.9) and the correlation probability for entangled photons pairs (1.71) are of the same functional form (assume that a polarization of one of the photons from the pair has been rotated by 90°) and support the BB84 protocol (see Sec. 1.21, p. 64)—as far as Alice and Bob are concerned—in an identical way. Therefore, by putting a source of entangled singlet-like photon pairs midway between Alice and Bob we can double the distance limit. It would be better that Alice keep the source and that the distance is increased by quantum repeaters (see Sec. 3.1.7, p. 151) because a single photon from a pair does not carry any information and cannot be eavesdropped.

The entangled pair implementations have mostly been carried out by means of parametric down-conversion (the inverse of parametric generation). Parametric down-conversion is a quantum effect in nonlinear optics.

[8]For the fourth implementation—continuous variables—we direct the reader to [Bennett et al., 2004].

In Sec. 1.8 (p. 17) we dealt with linear polarization

$$\mathbf{P} = \varepsilon_0 \chi \mathbf{E}, \tag{2.112}$$

where ε_0 is the vacuum permittivity and χ the electric susceptibility. In a nonlinear medium, an intense electric field of one frequency can generate nonlinear polarization at other frequencies. Then the outgoing polarizations $\mathbf{P}=[P_1, P_2, P_3]^T$ become nonlinear with respect to the electric field $\mathbf{E}=[E_1, E_2, E_3]^T$:

$$\mathbf{P} = \varepsilon_0(\chi^{(1)}\mathbf{E} + \chi^{(2)}\mathbf{E}^2 + \dots), \tag{2.113}$$

where $\chi^{(1)}$ is the first ordered (birefringent) electric susceptibility (a 3×3 tensor), $\chi^{(2)}$ is the second ordered electric susceptibility (media lacking a center of symmetry), etc. The first term in Eq. (2.113) reads

$$\varepsilon_0 \begin{bmatrix} \chi_{11} & \chi_{12} & \chi_{13} \\ \chi_{21} & \chi_{22} & \chi_{23} \\ \chi_{31} & \chi_{32} & \chi_{33} \end{bmatrix} \begin{bmatrix} E_1 \\ E_2 \\ E_3 \end{bmatrix} \tag{2.114}$$

(it describes, for example, the birefringent plates we used in Sec. 1.21, Fig. 1.27), the second term is

$$\varepsilon_0 \begin{bmatrix} \sum_{j,k=1}^{3} \chi^{(2)}_{1jk}(\omega_1, \omega_2, \omega_3) E_j E_k \\ \sum_{j,k=1}^{3} \chi^{(2)}_{2jk}(\omega_1, \omega_2, \omega_3) E_j E_k \\ \sum_{j,k=1}^{3} \chi^{(2)}_{3jk}(\omega_1, \omega_2, \omega_3) E_j E_k \end{bmatrix}, \tag{2.115}$$

where $\chi^{(2)}_{ijk}$ is a second rank tensor with 27 components, etc.

In the parametric down-conversion, one photon of frequency ω_0, called the *pump photon*, is incident on the nonlinear media (birefringent dielectric having the above $\chi^{(2)}$ susceptibility) and polarized along a chosen axis (say $\mathbf{P}_{\text{in}} = [P_1, 0, 0]$, which we will call *extraordinary* polarization). The pump photon breaks up into two photons of lower frequencies, ω_1 and ω_2, called the *signal photon* and the *idler photon*, respectively, where $\omega_1 \geq \omega_2$. The process of conversion is a nonlocal process in the sense that the position within a crystal from where the signal and idler photons emerge is not (and theoretically cannot be) determined. As a consequence, although both signal and idler appear together within femtoseconds, a pinhole that lets one of them through cannot precisely determine the direction of the other (the position of another pinhole which would let the other photon through). For pinholes of equal size this results in efficiency of about 0.05.

Energy ($E = h\nu$) conservation yields

$$E_0 = E_1 + E_2 \qquad \Rightarrow \qquad \omega_0 = \omega_1 + \omega_2, \tag{2.116}$$

while momentum conservation implies the phase-matching condition

$$\mathbf{p}_0 = \mathbf{p}_1 + \mathbf{p}_2 \quad \Rightarrow \quad \mathbf{k}_0 = \mathbf{k}_1 + \mathbf{k}_2, \tag{2.117}$$

where $\mathbf{k}$ is the wave vector

$$\mathbf{k} = \frac{n\omega}{c}\mathbf{s}, \tag{2.118}$$

where n is the index of refraction, c the speed of light, and $\mathbf{s}$ a unit vector.

For the uniaxial case (only one optical axis), we distinguish two major types of outgoing photons according to their polarizations:

- *Type-I down-conversion.* The pump photon from a strong laser pump beam is extraordinarily (say, vertically) polarized; the signal and idler photons are ordinarily (horizontally) polarized.
- *Type-II down-conversion* The pump and idler are extraordinarily polarized; the signal photon is ordinarily polarized.

Depending on the crystals we choose, we can obtain the coaxial and intersecting signal-idler cones as shown in Fig. 2.18. Various KDP crystals—for example, AgGaSe2—are used for type-I down-conversion. BBO crystals, beta-barium-borate or β-BaB_2O_4, are typically used for type-II down-conversion.

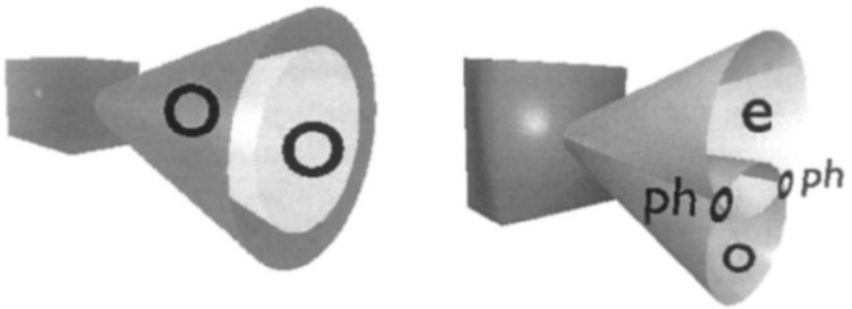

Figure 2.18. Typical type-I (left) and type-II (right) down-converted signal-idler cones. o (e) are ordinary (extraordinary) photon cones. ph are the pinholes through which we let the photon pairs into fibers.

When $|\mathbf{k}_1| = |\mathbf{k}_2|$, the color (frequency) of the signal photon is equal to the color of the idler photon (half of the frequency of the pump photon) (see Eq. (2.116)). We achieve this outcome for a particular angle that

the wave vector of the pump photon $\mathbf{k}_0$ makes with the optical axis of the crystal. Then the signal and idler photons appear at the opposite sides of the line determined by $\mathbf{k}_0$, as shown in Fig. 2.19 (a) and (c).

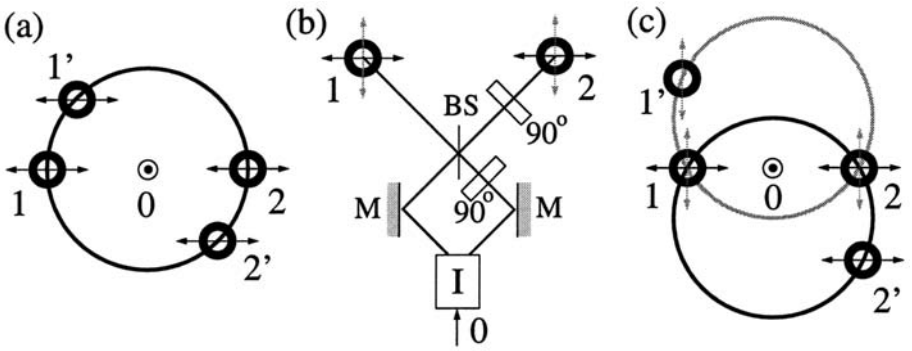

Figure 2.19. (a) Type-I down-conversion for the signal and idler of the same frequency; the cones coincide; pinholes 1–2 and 1'–2' let through the ordinary signal and idler that appear at the opposite sides of the line 0 determined by the pump wave vector $\mathbf{k}_0$; (b) EPR pair generation by means of type-I down-conversion: after the signal and idler of the same frequency interfere at the beam splitter BS, they appear entangled in a singlet-like state at pinholes 1–2; (c) EPR pair generation by means of type-II down-conversion: for the signal and idler of the same frequency the cones intersect and pinholes 1–2 let through the signal and idler entangled. Photons coming out of 1'–2' cannot entangle.

Both type-I and type-II down-converted photons can be used for the polarization-coding of entangled, EPR pairs for the BB84 protocol. With type-I down-conversion, as shown in Fig. 2.19 (b), after we rotate, say, the idler by 90°, let the signal and idler combine at a beam splitter, rotate one of the outgoing photons by 90°, and let the photons through the polarizers, according to Eq. (1.80), we get

$$\langle \Psi_t | \mathcal{D}_2^\dagger \mathcal{D}_1^\dagger \mathcal{D}_1 \mathcal{D}_2 | \Psi_t \rangle = \frac{1}{2} \sin^2(\theta_1 - \theta_2 - \frac{\pi}{2}) = \frac{1}{2} \cos^2(\theta_1 - \theta_2), \qquad (2.119)$$

where Ψ_t is the triplet entangled state

$$|\Psi_t\rangle = \frac{1}{\sqrt{2}}(|0\rangle_1 |0\rangle_2 + |1\rangle_1 |2\rangle_2) \qquad (2.120)$$

that corresponds to probability (2.119).

With type-II down-conversion, as shown in Fig. 2.19(c), photons passing through the pinholes 1 and 2 also appear entangled because one cannot know which cone which photon comes from [Kwiat et al., 1995].

We see that the probability (2.119) equals the Malus law probability (1.9), so the BB84 protocol—for Alice and Bob—remains the same as

presented in Sec. 1.21. However, Eve is here at a disadvantage. In Sec. 1.21 (p. 64), Alice prepares photons and sends them to Bob. As we already emphasized in Sec. 1.23 (p. 81) and in this section above, if Alice prepares photons with a polarizer and sends more than one photon per time window, these photons will all be prepared in the same way, and Eve can copy them unnoticed. If Alice and Bob use the entangled photons coming from a common source which is with Alice, then the photons Eve can catch are genuinely random, and she cannot obtain any information from them. Nevertheless, they are entangled with the photons Alice possesses and can be teleported to Bob by means of quantum repeaters (see Sec. 3.1.7, p. 151) The disadvantage of such a scheme is that the whole device is much more demanding, and proper quantum repeaters still have not been realized in a laboratory. Besides, there is a problem with both Alice and Bob catching one photon but from two different pairs within a single time window.[9] In this case the corresponding bit is wrong and they cannot find out what it is without applying the error correction scheme.

In a realistic entangled pair implementation, a phase-coding scheme will most probably again prevail (see Sec. 1.23, p. 81), since polarization is not robust enough to allow implementation over larger distances. One such scheme, according to Franson [Franson, 1989] and Tapster, Rarity, and Owens[Tapster et al., 1994], is shown in Fig. 2.20.

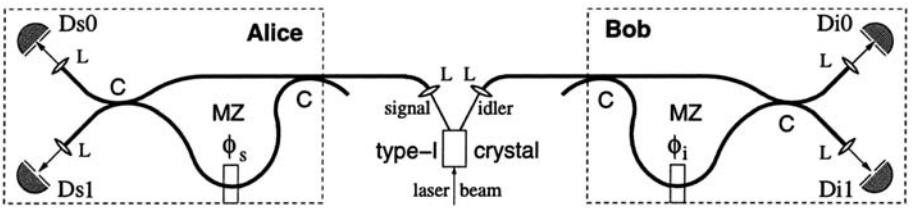

Figure 2.20. Phase-coding of entangled, EPR pair implementation of quantum key distribution according to [Tapster et al., 1994]. Fiber couplers C behave like beam-splitters and build Mach–Zehnder interferometers, MZ, on each side. Phase shifters ϕ_s and ϕ_i balance the MZs. Lenses L collect photons to the fibers and direct them towards the detectors.

The phase-coding scheme presented is based on the indistinguishability of Mach–Zehnder interferometer routes. Events where both photons pass through the long arms of the interferometer and those where they

[9] We could significantly reduce the number of such cases using two sources and double entanglement analogous to the one shown in Fig. 1.25 (p. 59) and pinholes for photons 1 and 2, say five times bigger than for photons 3 and 4 [Pavičić, 1997]. However, that would also slow down the transmission rate.

pass through the short arms cannot be distinguished from each other because the moment in which the signal and idler are down-converted is uncertain. However, when the down-conversion occurs, it occurs within femtoseconds, and we can distinguish (by precise time-of-flight measurements) the events where one photon takes the long arm and the other the short one and discard them. In a manner similar to polarization, we can calculate the coincidence rate between Ds1 and Di1 to be proportional to $\cos^2(\phi'_1 - \phi'_2)$, where ϕ' depends on the phase shift ϕ and the path length difference (cf. Fig. 1.32, p. 81 and Table 1.8, p. 82).